A flashing flow model for the rapid depressurization of CO_2 in a pipe accounting for bubble nucleation and growth

Alexandra Metallinou Log[b,*], Morten Hammer[a], Svend Tollak Munkejord[a]

[a] *SINTEF Energy Research, P.O. Box 4761 Torgarden, NO-7465 Trondheim, Norway*
[b] *Norwegian University of Science and Technology, Department of Energy and Process Engineering, NO-7491 Trondheim, Norway*

Abstract

Flashing flow is encountered in many industrial systems involving nozzles, valves and decompression of vessels and pipes. In the context of CO_2 capture and storage (CCS), the design of safe and efficient CO_2 transportation systems requires accurate flashing models, e.g., for safety analysis of pipe fractures and to predict the mass flow through relief valves. We propose a homogeneous flashing model (HFM) for flashing flow accounting for the underlying physical phenomena of the phase change: bubble nucleation, coalescence, break-up and growth. Homogeneous nucleation is modeled using classical nucleation theory and heterogeneous nucleation is approximated with constant rates of bubble creation and mass transfer from liquid to vapor. The flashing flow model is fitted for CO_2 pipe depressurization data at various initial conditions. We find that the same, constant model parameters can be applied for the whole set of depressurization cases considered, as opposed to the conventional homogeneous relaxation model which typically is tuned on a case-by-case basis. For depressurization paths where the fluid state passes close to the critical point, we demonstrate that an accurate description of the flashing process along the length of the pipe can only be achieved when both homogeneous and heterogeneous nucleation are accounted for.

Keywords: carbon dioxide, decompression, flashing, non-equilibrium, nucleation, vapor-liquid flows

*Corresponding author.
Email addresses: alexandra.m.log@ntnu.no (Alexandra Metallinou Log), alexandra.log@hotmail.com (Alexandra Metallinou Log)

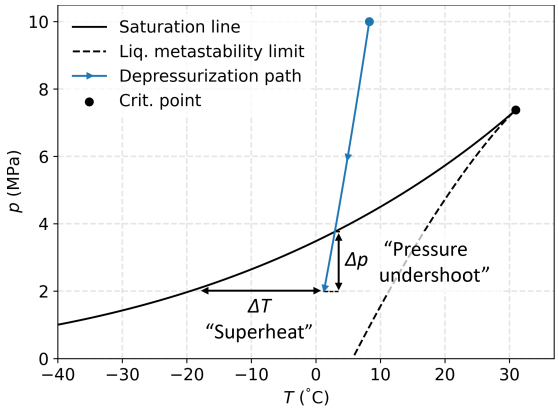

Figure 1: Illustration of a depressurization path in the liquid/dense liquid phase before flashing begins in a p-T diagram for CO_2. The superheat and pressure undershoot reached before flashing begins are indicated.

1. Introduction

1.1. Motivation

Flash boiling (flashing) is a phase change phenomenon that is triggered by the depressurization of a liquid below its saturation pressure. This phenomenon affects the operation and safety assessment of several industrial systems including pressurized water (nuclear) reactors, refrigeration systems and of main interest for the present work: CO_2 transportation pipelines in the context of CO_2 capture and storage (CCS). Scenarios where flashing may occur includes the opening of a pressure relief valve or accidents such as a pipe rupture (Klinkby *et al.*, 2011; Munkejord *et al.*, 2016; Pham and Rusli, 2016; Liao and Lucas, 2017b). In such scenarios, the flashing process determines the resulting pressure, temperature, speed of sound and outflow rate of the fluid. It is therefore important to model flashing flows accurately.

During a rapid depressurization event, the liquid state can pass far into its thermodynamically metastable region before significant flashing begins, producing a *pressure undershoot* and the liquid becomes *superheated* as illustrated in Figure 1. These are both measures of non-equilibrium. The non-equilibrium effects are strongly dependent on how bubbles nucleate and grow in the liquid. A better understanding of the underlying phenomena during flashing, such as bubble nucleation and growth, can benefit industrial applications both in terms of optimizing their efficiency and ensuring their safe operation.

The present work is particularly motivated by the need to develop accurate models to ensure that an initial puncture or crack in a CO_2-carrying pipeline will not develop into a *running ductile fracture* (RDF). RDF is a phenomenon where a defect in a pipe develops into a crack that propagates along the pipe, driven by the pressure forces of the escaping fluid (Cosham *et al.*, 2014; Aursand *et al.*, 2016a; DNV, 2021; Skarsvåg *et al.*, 2023). Thus, accurate modeling of the pressure evolution during depressurization is required to design RDF-resistant pipes. The pressure evolution during depressurization is in turn strongly affected by the flashing process. In large-scale fracture tests with CO_2 and CO_2-rich mixtures, the crack-tip pressure is found to be up to 20% lower than the saturation pressure, see, e.g., Michal *et al.* (2020). In previous work, we have shown that predictions of the crack-tip pressure can be improved by taking into account

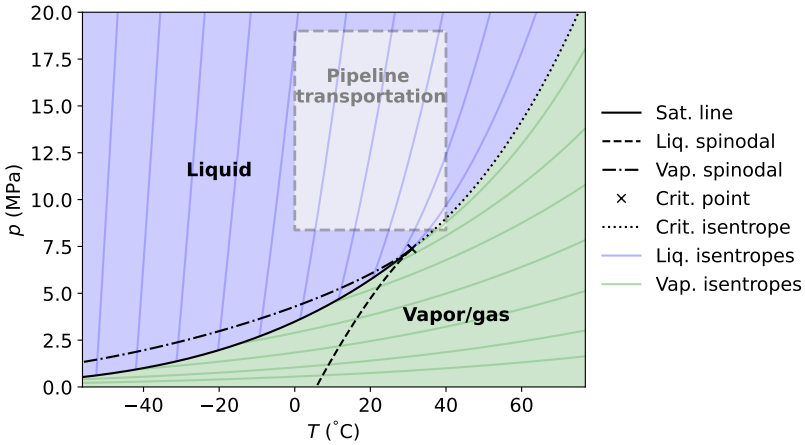

Figure 2: Phase diagram for CO_2 illustrating the present definition of liquid and vapor, and the relevant operating range for CO_2 pipeline transportation. Note that the liquid phase may exist in a metastable state up to the liquid metastability limit and vice versa for the vapor phase.

non-equilibrium flashing as compared to the homogeneous equilibrium model (HEM), which assumes equilibrium between the phases (Skarsvåg *et al.*, 2023).

For high-capacity CO_2-carrying pipelines, the CO_2 will typically be transported at supercritical pressures, and with an entropy below that of the critical point, providing a liquid-like behavior of the fluid. This state is often referred to as "dense phase", although the definition of the term varies somewhat, see, e.g., IPCC (2005, Chap. 4), Brownsort (2019) and Committee on Carbon Capture, Use, and Storage (2019). For simplicity, we will call these states *liquid* if an isentropic depressurization will bring them to flash boil as a liquid. Our present definition of the liquid phase is shown in Figure 2. In the figure we also show the (approximate) relevant operating range for high-capacity CO_2 pipelines. A part of the transcritical CO_2 refrigeration cycle will also be in this region, see, e.g., Ringstad *et al.* (2020). For transcritical CO_2 refrigeration cycles, flashing through an ejector device can be applied to regain lost work, making accurate modeling of flashing CO_2 valuable in order to optimize the system.

We have run a series of pipe depressurization tests for pure CO_2 in the relevant operating range for CO_2 pipelines, with initial temperatures from 10 °C to 40 °C and an initial pressure around 12 MPa (Munkejord *et al.*, 2020a; Log *et al.*, 2024). Note that for the warmer cases, an isentropic depressurization path will pass very close to the critical point of CO_2, whereas the colder cases pass further away. In this region of the phase diagram, the distance from the saturation curve to the metastability limit increases significantly as the temperature decreases, see Figure 1. Therefore, the non-equilibrium effects during flashing vary considerably. To optimize the operation of and provide safety analyses for CO_2-carrying pipes, flow models should be able to predict these effects.

1.2. Typical depressurization results: importance of mass transfer during flashing

In Figure 3, we show a typical pressure profile in a pipe filled with a liquid, initially at rest, during depressurization. As the pipe is depressurized, a rarefaction wave propagates into the pipe at the local speed of sound. When the pressure becomes low

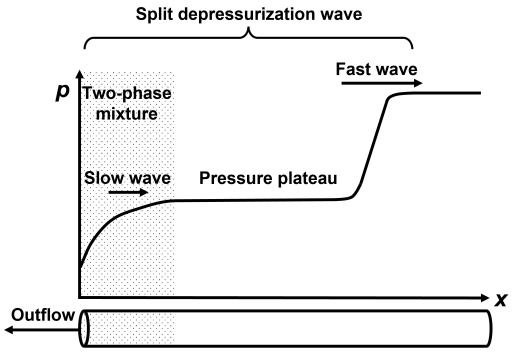

Figure 3: Illustration of a typical pressure profile for a depressurization wave in a pipe where flashing occurs. The flashing slows down the pressure wave significantly and causes the wave to split into a fast-moving part in the single-phase region and a slow-moving part in the two-phase region with a pressure plateau in-between.

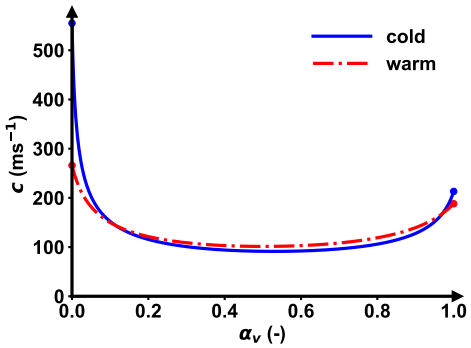

Figure 4: Computed variation in speed of sound with the vapor volume fraction for a saturated mixture of liquid–vapor CO_2 for a warm temperature ($T = 25.6\,°C$), relatively near the critical point, and for a colder temperature ($T = -2\,°C$). HRM* was used, see Section 2.2.

enough, the liquid starts flashing at the open end of the pipe. In Figure 4, we show how the speed of sound in a liquid-vapor mixture changes with the vapor volume fraction for the homogeneous chemical potential-relaxation model, which is described in Section 2.2. As vapor is added to the flow, the mixture speed of sound decreases significantly. Therefore, the rarefaction wave splits into a slow-moving wave in the two-phase mixture and a fast-moving wave in the single-phase fluid, with a single-phase pressure plateau in-between.

The pressure evolution near the open end of the pipe is different for warmer and colder depressurization tests. As discussed in Log *et al.* (2024), if the depressurization path passes sufficiently close to the critical point of the fluid (i.e., within a few K/°C), we observe nearly no pressure undershoot or superheat before significant flashing begins. A typical pressure trace near the open end of the pipe for such a case is shown in Figure 5a. The pressure decreases quickly in the single-phase region until flashing begins nearly at the local saturation pressure. The depressurization continues at near saturation conditions until the flow chokes, i.e., the flow speed is equal to the local speed of sound. After this, the pressure decreases very slowly as the maximum flow rate has been reached. Such pressure evolutions have been observed in high-temperature depressurization experiments with pure CO_2, e.g., Test #31 of Botros *et al.* (2016), Test 6 of Munkejord *et al.* (2020a) and Test 24 of Log *et al.* (2024).

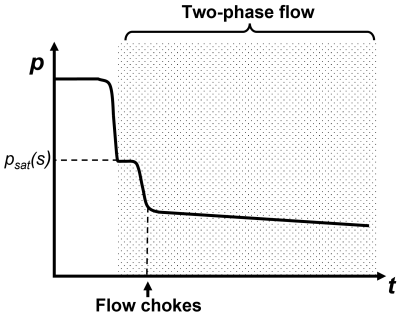

(a) Depressurization path passing close to the critical point.

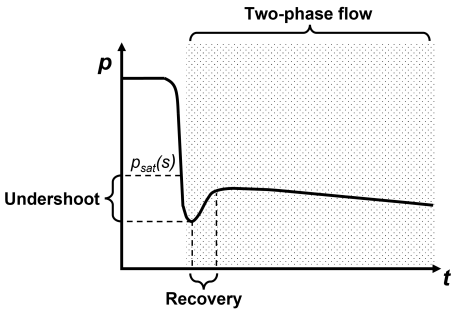

(b) Depressurization path passing further away from the critical point.

Figure 5: Illustrations of typical pressure traces near the open end of the pipe for depressurization cases where the depressurization path passes (a) close to or (b) further away from the critical point of the fluid.

For colder depressurization cases, we observe a clear pressure undershoot and recovery, as illustrated in Figure 5b. The pressure decreases quickly below the local saturation pressure, providing a pressure undershoot. The pressure then rebounds as flashing is initiated, the flow chokes abruptly and a slow pressure reduction follows while the fluid is in a two-phase mixture state. This kind of pressure evolution has been observed in several experiments for a variety of fluids including water (Edwards and O'Brien, 1970; Lienhard *et al.*, 1978; Barták, 1990), R-12 (Winters and Merte, 1979), pure CO_2 (Botros *et al.*, 2016; Munkejord *et al.*, 2020a; Log *et al.*, 2024) and CO_2-rich mixtures (Botros *et al.*, 2017a,b,c; Munkejord *et al.*, 2021). As illustrated in Figure 4, the speed of sound decreases more abruptly for colder depressurization cases when the flow transitions from pure liquid to a two-phase mixture. The pressure evolution in the pipe is therefore significantly affected once flashing begins. In order to capture the pressure evolution during depressurization in engineering tools, the mass-transfer rate from liquid to vapor must therefore be accurately modeled.

1.3. Background on mass-transfer models for flashing flows

A number of models have been developed to model flashing during depressurization. For detailed reviews, we refer the readers to Pinhasi *et al.* (2005); Liao and Lucas (2017a) and Liao and Lucas (2021). The mass-transfer models can be categorized into two types: the simpler HRM-type models and the more complex models which account for bubble nucleation. We provide a brief overview of the two types of mass-transfer models below.

1.3.1. HRM-type mass-transfer models

One of the more widely used and simple models which can reproduce the effect of a pressure undershoot is the homogeneous relaxation model (HRM) discussed by Bilicki and Kestin (1990). Here, the mass-transfer rate is modeled phenomenologically using a relaxation parameter multiplied by a driving force for the phase change. We will call this kind of mass-transfer model *HRM-type* models. Examples of other HRM-type mass-transfer models include those of Lee (1980), Saurel *et al.* (2008) and Liu *et al.* (2017).

Various correlations have been suggested for the relaxation parameter in HRM-type models for different initial conditions, e.g., the correlations of Downar-Zapolski *et al.* (1996) for water and Angielczyk *et al.* (2010); Log *et al.* (2024) for CO_2. These

correlations usually do not provide accurate results for other cases than the ones they are fitted to, and for low temperatures the correlation of Downar-Zapolski *et al.* (1996) has been found to predict non-physically large relaxation times (Liao and Lucas, 2021; Saha *et al.*, 2017). As we pointed out in Log *et al.* (2024), the mass-transfer model suggested by Liu *et al.* (2017) has been applied by several authors (Liu *et al.*, 2017, 2018; Flechas *et al.*, 2020; Xiao *et al.*, 2020) to test their flow models for CO_2 depressurization cases. This model is a modified version of the HRM-type mass-transfer model of Lee (1980) where the driving force of the mass transfer is based on the pressure undershoot as opposed to the liquid superheat. The Liu *et al.* (2017) model's relaxation parameter has been fitted to the pressure recordings of Test #32A of Botros *et al.* (2016), and the various authors have found an optimal value in the range $7\,s^{-1}$ to $15\,s^{-1}$. Even for a single depressurization test, there is no agreement on the value of the relaxation parameter.

More complex HRM-type mass-transfer correlations have also been developed. An example is the mass-transfer relation applied in the delayed equilibrium model (DEM) to predict critical flow in nozzles (Bartosiewicz and Seynhaeve, 2013, 2014; Seynhaeve *et al.*, 2015; De Lorenzo *et al.*, 2017). In this mass-transfer relation, two relaxation parameters are applied: one accounting for the time-scale of heterogeneous bubble nucleation and another accounting for the time-scale of bubble nucleation in the bulk of the fluid. The correlation has been fitted for water flashing flow tests (Bartosiewicz and Seynhaeve, 2013; Seynhaeve *et al.*, 2015). However, the correlation was found to be unsuited for CO_2 flow in nozzles (Angielczyk *et al.*, 2019) when tested against the CO_2 nozzle flow data of Nakagawa *et al.* (2009). This was the case even with updated relaxation parameters fitted to the data. Angielczyk *et al.* (2020) later proposed a more complex correlation for CO_2, including an exponential term related to the convergence and divergence rates of the nozzle and an additional parameter for model tuning. With this model, they were able to fit the data better.

Though the HRM-type models are practical due to their simplicity, they generally lack predictive abilities and must be fitted to experimental data, typically on a case-by-case basis. For the safety evaluation of pipelines, it is necessary to make *predictive* estimates for various pipe configurations and flow compositions. To this end, mass-transfer models which account for the physical processes that occur during flashing are needed. These processes include bubble nucleation, bubble breakup, coalescence and growth. The reviews of Pinhasi *et al.* (2005); Liao and Lucas (2017a) and Liao and Lucas (2021) provide details on the challenges and progress in modeling these terms. A main challenge remains in predicting the nucleation of bubbles in the flow.

1.3.2. Models accounting for bubble nucleation

There are two main types of bubble nucleation: homogeneous and heterogeneous. Homogeneous nucleation occurs in the bulk of the fluid and is caused by random density fluctuations creating vapor-like volumes that – if they are large enough – become their own stable phase and grow (Debenedetti, 1997). In order for bubbles to form in this manner, a certain energy barrier must be overcome. This energy barrier decreases near the critical point of the fluid, and larger bubble nucleation rates are expected. The nucleation rate and mass-transfer caused by homogeneous nucleation can be estimated using classical nucleation theory (CNT). CNT has been found to work well in estimating the superheat limit of CO_2 (Aursand *et al.*, 2016b; Wilhelmsen and Aasen, 2022) and water (Wilhelmsen and Aasen, 2022) for temperatures near the critical point.

Heterogeneous nucleation occurs on surfaces of, e.g., suspended impurities or confining walls. There are two main methods currently being applied to model hetero-

geneous nucleation. The first method involves the assumption that the mechanism of nucleation is still governed by random density fluctuations, but with a decreased energy-barrier for the bubble formation (Alamgir and Lienhard, 1981; Barták, 1990; Deligiannis and Cleaver, 1990, 1992; Elias and Chambré, 1993; Banasiak and Hafner, 2013; Wilhelmsen and Aasen, 2022). The second method is based on the assumption that the nucleation occurs on trapped vapor seeds on these surfaces, see, e.g., the *crevice model* (Bankoff, 1958; Apfel, 1970; Atchley and Prosperetti, 1989; Chappell and Payne, 2007). Some authors refer to the latter form of nucleation as *wall nucleation* (Liao and Lucas, 2017a).

Although investigations have been made for heterogeneous nucleation on ideally flat surfaces (Debenedetti, 1997; Gallo *et al.*, 2021) and conical crevices (Wilt, 1986), to our knowledge, an accurate, predictive model for heterogeneous bubble nucleation in real systems does not yet exist. Models for heterogeneous nucleation in real systems are therefore typically correlated to experimental data. See, e.g., Alamgir and Lienhard (1981); Barták (1990); Deligiannis and Cleaver (1990, 1992); Elias and Chambré (1993); Banasiak and Hafner (2013); Wilhelmsen and Aasen (2022) for correlations of the reduction factor for the energy of bubble formation and Kocamustafaogullari and Ishii (1983); Shin and Jones (1993); Blinkov *et al.* (1993); Hibiki and Ishii (2003) for correlations for wall nucleation. Most correlations based on a reduction factor for the energy of bubble formation are fitted to match a chosen critical nucleation rate to the recorded superheat limit or maximum pressure undershoot observed in experiments. Consequently, the reduction factor based nucleation models tend to predict the superheat limit and expected maximum pressure undershoots well. However, these models are rarely used in flow models to predict the mass transfer during flashing.

An example of a reduction factor based nucleation model being applied to model the mass transfer during the depressurization of a pipe can be found in Riznic and Ishii (1989). With this mass-transfer model, the predicted pressure became much too low over time after the pressure undershoot had occurred as compared to experimental results. Riznic and Ishii (1989) therefore suggested that some other nucleation process was keeping the pressure elevated over time.

Heterogeneous nucleation models based on the assumption of wall nucleation tend to perform better in flashing flow models, see, e.g., Shin and Jones (1993); Blinkov *et al.* (1993). Models assuming a constant number of bubble seeds in the flow also tend to match experimental data quite well, see, e.g., Winters and Merte (1979) for the simulation of R-12 depressurization tests and Ivashnyov *et al.* (2000) for the simulation of the Edwards and O'Brien (1970) water depressurization tests. Winters and Merte (1979) applied a discharge coefficient $C_d < 1$ at the open end to match the experimental results, but Ivashnyov *et al.* (2000) found that this was not needed when bubble breakup was accounted for in the flow. The models assuming that vapor seeds initiate the flashing typically ignore the effect of homogeneous bubble nucleation. In fact, homogeneous nucleation is often deemed irrelevant when modeling flashing flows, see, e.g., Liao and Lucas (2017a), though this is likely based on the assumption that the depressurization will occur far away from the critical point of the fluid.

1.4. Present contribution and overview of paper

For the relevant operating region of CO_2 pipelines and refrigeration systems, homogeneous nucleation will be non-negligible. Wilhelmsen and Aasen (2022) showed that for flashing flows near the critical point there is a transition from the maximum attainable superheat being determined by homogeneous nucleation for warmer cases and heterogeneous nucleation for colder cases. The same trend can be found for our

pipe depressurization tests (Log *et al.*, 2022, 2024). Flow visualization experiments of CO_2 depressurizations show that bubbles tend to form on the wall of the test section as well, suggesting that heterogeneous nucleation plays an important role in the flashing process (Hansen *et al.*, 2019). It is not clear how homogeneous and heterogeneous nucleation affect the resulting flow during depressurization. We further hypothesize that including the effect of homogeneous nucleation in flashing flow models will improve their predictive ability.

The purpose of the present work is therefore to develop and study a flashing flow model where both homogeneous and heterogeneous bubble nucleation is accounted for. We also include simple models for bubble growth, coalescence and breakup. The model fit to experiments with pure CO_2 (Munkejord *et al.*, 2020a; Log *et al.*, 2024) is assessed and the effect of the two nucleation modes on the flashing process is studied. The results are further compared to predictions of a non-equilibrium flow model with a HRM-type mass-transfer model, and the homogeneous equilibrium model, to illustrate the deviation from equilibrium of the experiments and non-equilibrium models.

The remainder of the article is structured as follows. Section 2 presents the flow models and Section 3 presents the main mass-transfer model studied in the present work. Then, we describe the numerical solution method for the governing equations in Section 4. In Section 5, we assess the model fit to the experimental pressure recordings, and discuss the effect of homogeneous and heterogeneous nucleation. We finally provide a summary and concluding remarks in Section 6.

2. Flow models

In this section, we outline the flow models applied in the present work: the homogeneous equilibrium model, the homogeneous chemical-potential relaxation model with HRM-type mass-transfer and the novel homogeneous flashing model. In Section 2.4, we outline our models for wall friction and heat transfer through the pipe wall. In Section 2.5, the initial and boundary conditions are described, and in Section 2.6 the thermophysical modeling of the fluid is described. Details on our mass-transfer model for the homogeneous flashing model are provided in the next section, Section 3.

All the flow models employed in this work are based on the assumption that the flow is homogeneous, i.e., that all phases are advected with the same velocity. This is a reasonable assumption if the phases are dispersed. Flow visualization experiments show that this assumption is reasonable for the time-scales considered here (0 ms to 20 ms) (Brown *et al.*, 2013, 2014; Quinn *et al.*, 2022).

2.1. The homogeneous equilibrium model

In the HEM it is assumed that all phases are advected at the same velocity and are in mechanical, thermal and chemical equilibrium. The model is therefore mainly applicable for multiphase dispersed flow where the time-scale of pressure exchange, heat transfer and mass transfer between the phases is much shorter than the characteristic time-scales of the flow. The governing equations of the HEM take the form of the 1D Euler equations for single-phase compressible inviscid flow, with a mass conservation

equation, a momentum balance equation and an energy balance equation:

$$\frac{\partial \rho}{\partial t} + \frac{\partial (\rho u)}{\partial x} = 0, \tag{1}$$

$$\frac{\partial (\rho u)}{\partial t} + \frac{\partial (\rho u^2 + p)}{\partial x} = \rho g_x - \mathcal{F}, \tag{2}$$

$$\frac{\partial E}{\partial t} + \frac{\partial ((E + p)u)}{\partial x} = \mathcal{Q}. \tag{3}$$

Here, $\rho = \alpha_v \rho_v + \alpha_\ell \rho_\ell$ is the density of the vapor (v) and liquid (ℓ) mixture, u is the mixture velocity, p the pressure and E the total energy of the mixture.

$$E = \rho \left(e + \frac{1}{2} u^2 \right), \tag{4}$$

where $e = (\alpha_v \rho_v e_v + \alpha_\ell \rho_\ell e_\ell)$ is the specific internal energy of the mixture and α_k denotes the volume fraction of phase $k \in v, \ell$. $\mathcal{F}$ is the pipe wall friction and $\mathcal{Q}$ is the heat transferred through the pipe wall. g_x is the gravitational acceleration in the axial direction of the pipe. We assume that the pipe is completely horizontal such that $g_x = 0$.

2.2. The homogeneous chemical potential-relaxation model

For certain transient flow processes, such as depressurization, the time-scale of mass transfer from liquid to vapor is too slow to maintain equilibrium between the phases. In order to model the flow accurately for such cases, the equilibrium assumptions must be relaxed. The homogeneous chemical potential-relaxation model, HRM*, keeps the assumptions of the HEM with the exception that chemical non-equilibrium between the phases is allowed. Note that other authors denote this model differently, such as the "temperature equilibrium model" (Le Martelot *et al.*, 2014), the "pressure-temperature relaxation model" (Lund, 2012) and the "four-equation pT-relaxed model" (Pelanti, 2022).

The HRM* consists of four equations describing the mass balance of vapor, mass balance of liquid, the conservation of momentum for the two-phase mixture and the conservation of total energy for the mixture:

$$\frac{\partial (\alpha_v \rho_v)}{\partial t} + \frac{\partial (\alpha_v \rho_v u)}{\partial x} = \Gamma, \tag{5}$$

$$\frac{\partial (\alpha_\ell \rho_\ell)}{\partial t} + \frac{\partial (\alpha_\ell \rho_\ell u)}{\partial x} = -\Gamma, \tag{6}$$

$$\frac{\partial (\rho u)}{\partial t} + \frac{\partial (\rho u^2 + p)}{\partial x} = \rho g_x - \mathcal{F}, \tag{7}$$

$$\frac{\partial E}{\partial t} + \frac{\partial ((E + p)u)}{\partial x} = \mathcal{Q}, \tag{8}$$

where Γ is the mass-transfer rate between the phases. For an infinitely fast mass-transfer rate, the HRM* relaxes to the HEM.

The mass-transfer rate, Γ, is modeled with the standard HRM-term (Bilicki and Kestin, 1990):

$$\Gamma = \rho \frac{y_{g,\text{eq}} - y_v}{\theta}, \tag{9}$$

where $y_v = \dfrac{\alpha_v \rho_v}{\rho}$ is the mass fraction of vapor, $y_{v,\text{eq}}$ is the equilibrium mass fraction of vapor and θ is a relaxation time > 0. In our previous work (Log *et al.*, 2024), we

derived a correlation for the relaxation time fitting the maximum pressure undershoots observed for a series of pipe depressurization experiments with CO_2 (Munkejord *et al.*, 2020a; Log *et al.*, 2024) listed in Table 1, with the exception of Test 25:

$$\theta = 3.165\,\mathrm{ms}\left[1 - \exp\left(-33.283\Delta\tilde{s}_0^{4.014}\right)\right]. \tag{10}$$

Here,

$$\Delta\tilde{s}_0 = \frac{s_0 - s_c}{s_{\mathrm{tr}} - s_c} \tag{11}$$

is the scaled, relative initial entropy and s_0 is the initial entropy before the depressurization begins, s_c is the critical point entropy and s_{tr} is the triple point entropy.

Though the relaxation time can be fitted to experiments, it does not account for all the complex processes which occur during flashing.

2.3. The homogeneous flashing model

In this section, we summarize the flow equations of the homogeneous flashing model (HFM). The HFM is based on the governing equations of the HRM*, (5)–(8), however, the term describing the mass-transfer between the liquid and vapor phase, Γ, is modeled taking into account different kinds of bubble nucleation in addition to bubble growth through evaporation, bubble breakup and coalescence. The details of the mass-transfer model in the HFM are presented in Section 3.

Evaporation causes a flux of mass transfer through a liquid–vapor surface. In order to model the mass transfer due to evaporation, it is necessary to recover information on the interfacial area density between the liquid and vapor phases. We therefore include additional transport equations for the bubble number density in the flow and interfacial area separating the liquid and vapor. The bubble transport equation is

$$\frac{\partial n_{\mathrm{bub}}}{\partial t} + \frac{\partial (n_{\mathrm{bub}} u)}{\partial x} = J_{\mathrm{bub}}, \tag{12}$$

where n_{bub} is the number density of bubbles in the flow and J_{bub} is the creation or destruction rate of bubbles in the flow. The transport of interfacial area density is given by

$$\frac{\partial a_{\mathrm{int}}}{\partial t} + \frac{\partial (a_{\mathrm{int}} u)}{\partial x} = S_a, \tag{13}$$

where a_{int} is the interfacial area density separating liquid and vapor and S_a denotes the creation or destruction rate of interfacial area. S_a is either provided implicitly based on the creation rate of bubbles, or conservation is assumed, such that $S_a = 0$. Details on the estimate of the interfacial area density are given in Section 3.4.

2.4. Heat transfer and friction

For all the flow models above, the wall friction is calculated using the Friedel (1979) correlation and the heat transferred through the pipe wall is calculated by solving the heat equation in the radial direction in a two-layer domain, as described by Aursand *et al.* (2017). The in-pipe heat-transfer coefficient is estimated based on the Dittus–Boelter correlation, see, e.g. Bejan (1993, Chap. 6) and the outside heat-transfer coefficient is estimated to be $4\,\mathrm{W\,m^{-2}\,K^{-1}}$. To account for the enhanced heat transfer due to boiling/flashing at the wall, the correlation of Gungor and Winterton (1987) is applied for its simplicity. For more details on the friction and heat-transfer modeling, see Munkejord *et al.* (2021).

2.5. Initial and boundary conditions

The flow models were applied to simulate pipe depressurization experiments. For these experiments, we assume that the fluid is initially stationary, $u = 0$, and that it has a uniform pressure distribution, $p = p_{\text{init}}$. The initial temperature profile along the pipe is set based on recorded initial temperatures in the pipe using linear interpolation. As the initial condition for all cases considered here are fully in the liquid phase, $\alpha_{v,\text{init}} = 0$. For the initial condition of the pipe wall temperature, the steady state temperature is calculated based on the initial fluid temperature and the ambient temperature outside the pipe. The governing equations for the heat transfer are described by Aursand *et al.* (2017).

At the left end of the pipe, $x = 0$, the pipe is assumed to be fully open to the outside where $p = p_{\text{atm}}$. The numerical method applied to estimate the flow at the open end of the pipe is briefly summarized in Section 4, and details can be found in Log *et al.* (2024). At the right end of the pipe, the pipe has a closed wall. However, in the present work, the simulation times are too short for pressure waves to reach this region.

2.6. Thermophysical property models

The thermodynamic properties of the two-phase mixture are obtained with our in-house framework (Wilhelmsen *et al.*, 2017) using the GERG-2008 (Kunz and Wagner, 2012) equation of state (EOS). An open source version of the thermodynamic library can be found at GitHub (Hammer *et al.*, 2023). The EOS is used to calculate the densities and energies of the existing phases in both the stable and metastable region. The metastability limit or *spinodal* curve of the liquid phase is calculated based on

$$\left(\frac{\partial p_\ell}{\partial \rho_\ell}\right)_{T_\ell} = 0, \tag{14}$$

which is defined by the EOS.

3. Mass transfer in the homogeneous flashing model

In the present work, we model the mass-transfer rate, Γ, for the HFM as the sum of three terms: homogeneous nucleation, heterogeneous nucleation and evaporation through the liquid–vapor interface of bubbles in the flow:

$$\Gamma = \Gamma_{\text{hom}} + \Gamma_{\text{het}} + \Gamma_{\text{evap}}. \tag{15}$$

The bubble source term in the transport equation for bubbles (12), J_{bub}, is modeled in a similar way

$$J_{\text{bub}} = J_{\text{hom}} + J_{\text{het}} + J_{\text{break}} + J_{\text{coal}}, \tag{16}$$

where subscript 'break' denotes bubble breakup and subscript 'coal' stands for coalescence of bubbles. J_{coal} is modeled implicitly by limiting the bubble surface area in a control volume when a certain threshold for α_v is reached, as suggested by Pinhasi *et al.* (2005). We present the details on the modeling of each of the terms in the following sections.

3.1. Homogeneous nucleation

Homogeneous nucleation describes the formation of embryos of a new phase within a mother phase through random thermal fluctuations. Classical nucleation theory provides a formal estimate on the nucleation rate of critically-sized embryos through random density fluctuations. Here, *critically-sized* refers to the size where the embryo is just large enough not to collapse back to the mother phase. The derivation of this rate is thoroughly presented by Debenedetti (1997), and we here simply state the resulting equations. Note that we have presented similar descriptions of CNT in Hammer *et al.* (2022) and Skarsvåg *et al.* (2023), and it is re-stated here for completeness.

The nucleation rate (critically-sized embryos formed per volume and time) is defined as an Arrhenius-type rate law,

$$J_{\text{hom}} = K \exp\left(-\frac{\Delta G^*}{k_{\text{B}} T_\ell}\right), \tag{17}$$

where ΔG is the free-energy barrier of embryo formation, k_{B} is the Boltzmann constant and K is a kinetic prefactor. The superscript $*$ denotes properties of a critically-sized embryo. For the formation of bubbles in a superheated liquid, the free-energy barrier is estimated to be

$$\Delta G^* = \frac{4\pi\sigma r^{*2}}{3}, \tag{18}$$

where σ denotes the surface tension and r the radius of the bubble. It is assumed that the surface tension of the bubble, σ, is equal to the macroscopic surface tension of a planar interface between the liquid and vapor at equilibrium (Aasen *et al.*, 2023). We use the correlation of Rathjen and Straub (1977) to model the surface tension of CO_2.

The critical radius of the bubble is approximated as

$$r^* = \frac{2\sigma}{p_{\text{sat}}(T_\ell) - p_\ell}, \tag{19}$$

where $p_{\text{sat}}(T_\ell)$ is the saturation pressure at the temperature of the liquid. The kinetic prefactor can be approximated as

$$K = \tilde{\rho}_\ell \sqrt{\frac{2\sigma}{\pi m}}, \tag{20}$$

where m is the mass of one molecule and $\tilde{\rho}_\ell = \rho_\ell / m$ is the number density of molecules in the liquid. The mass-transfer rate from liquid to vapor due to homogeneous nucleation of bubbles is then estimated to be

$$\Gamma_{\text{hom}} = \rho_{g,\text{sat}}(T_\ell) V_{\text{bub}} J_{\text{hom}}, \tag{21}$$

where the volume of a critically-sized bubble is

$$V_{\text{bub}} = \frac{4}{3}\pi r^{*3}. \tag{22}$$

Assuming that the depressurization path in the liquid phase is isentropic, we can estimate the maximum attained superheat in pipe depressurization tests with pure CO_2. See, e.g., Log *et al.* (2022). In Figure 6, we compare the maximum attained superheat for CO_2 pipe depressurization experiments (Botros *et al.*, 2016; Log *et al.*, 2024), with a heat map of bubble nucleation rates predicted by CNT. For high temperatures,

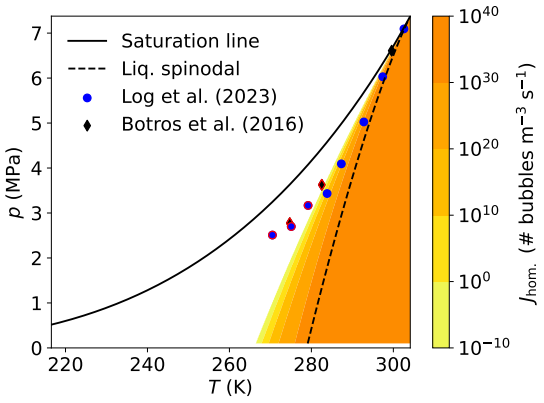

Figure 6: The homogeneous nucleation rate of critically-sized bubbles for CO_2 calculated using CNT with the GERG-2008 EOS, compared to the estimated maximum superheat observed in full-bore depressurization experiments (Log *et al.*, 2024; Botros *et al.*, 2016). The markers with red edges show points where the maximum superheat was reached in the experiments despite the homogeneous bubble nucleation rate calculated by CNT being lower than 10^{-10} bubbles m^{-3} s^{-1}.

the maximum attainable superheat coincides with regions where significant amounts of bubbles are nucleated as predicted by CNT. However, for colder depressurization cases, we observe five experiments where the maximum superheat is reached in a region where lower nucleation rates than $J_{\text{hom}} = 10^{-10}$ bubbles m^{-3} s^{-1} are predicted. This means that it should take over 316 years for a single, critically-sized bubble to form in a cubic meter of liquid CO_2, yet the experimental results suggest that flashing occurred. This deviation from CNT is observed for a variety of systems and fluids, and it is generally understood to be caused by *heterogeneous* bubble nucleation.

3.2. Heterogeneous nucleation

Heterogeneous nucleation refers to the formation of an embryo of a new phase within the mother phase on a surface, such as suspended impurities or a confining wall. As described in the introduction, there are currently two main methods being applied to estimate heterogeneous nucleation for flashing or boiling liquids. One method is based on the assumption that the bubbles form through density fluctuations with a reduced activation energy. The nucleation rate then becomes similar to CNT, but with the activation energy multiplied by a reduction factor between 0 and 1.

Expressions for the reduction factor has been derived for ideally flat surfaces and conical cavities, depending on knowledge of the contact angle of the fluid on the surface (Debenedetti, 1997; Wilt, 1986). However, these estimates fail to reproduce the superheat limits obtained during flashing in real (non-ideal) systems, see, e.g., Deligiannis and Cleaver (1990); Elias and Chambré (1993). To fit experimental data at low reduced temperatures, the reduction factor for the activation energy must be as small as 10^{-7} and 10^{-6} (Deligiannis and Cleaver, 1990; Elias and Chambré, 1993; Wilhelmsen and Aasen, 2022). The other method, denoted the crevice model or wall nucleation, assumes that the nucleation is aided by trapped bubbles in crevices providing a surface for the liquid to evaporate into (Bankoff, 1958; Apfel, 1970; Atchley and Prosperetti, 1989; Chappell and Payne, 2007). The trapped vapor seeds are denoted as *nucleation sites*.

We base our present model on the assumptions of the crevice model. However, we do not wish to derive complex correlations of the kind that have been developed for

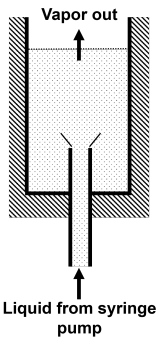

Figure 7: Illustration of evaporation system where vapor is withdrawn from the cell at the same rate as liquid is being supplied. The interface between the phases is assumed to be perfectly flat.

water, e.g., Kocamustafaogullari and Ishii (1983); Shin and Jones (1993); Blinkov *et al.* (1993); Hibiki and Ishii (2003). For simplicity, we assume that there exist a number of "perfect" nucleation sites in the pipe and that these nucleation sites provide a constant rate of mass transfer from liquid to vapor if the liquid is superheated. Similarly we also assume a constant rate of bubbles being produced due to the heterogeneous nucleation. The mass-transfer rate and bubble creation rate are then simply modeled as:

$$\Gamma_{\text{het}} = K_m, \text{ and } J_{\text{het}} = K_b. \tag{23}$$

We choose K_m and K_b as constant values fitted as well as possible to our CO_2 depressurization experiments, as reported in Section 5.2. This model for heterogeneous nucleation is not predictive, as opposed to the model for homogeneous nucleation.

3.3. Evaporation through bubble growth

Once bubbles have formed through nucleation, we assume that rapid evaporation will take place at the bubble surface. Most authors assume that the evaporation through the bubble surface is governed by heat transfer between the phases, see, e.g., Winters and Merte (1979); Blinkov *et al.* (1993); Ivashnyov *et al.* (2000); Liao and Lucas (2017a). In the present work, we assume that evaporation is driven by the difference in chemical potential between the liquid and vapor phases, and estimate the evaporation flux using linear non-equilibrium thermodynamics coupled with kinetic theory as described in Kjelstrup and Bedeaux (2008), Chapter 11.

Consider a partially filled funnel with a liquid–vapor interface, where liquid is continuously supplied from the bottom as evaporation takes place such that the interface remains stationary, as illustrated in Figure 7. We ignore viscous effects and assume a constant pressure in the system. Furthermore, the surface is regarded as flat on a molecular scale. As described in more detail in Chapter 11 of Kjelstrup and Bedeaux (2008), the mass-transfer rate through the interface during evaporation or condensation can be estimated as

$$\frac{\Gamma_{\text{evap}}}{a_{\text{int}}} = \frac{1}{R^{s,\ell}_{\mu\mu} + R^{s,v}_{\mu\mu}} \frac{\mu_\ell - \mu_v}{T}, \tag{24}$$

where μ_k denotes the chemical potential of phase $k \in \{\ell, v\}$, $R^{s,\ell}_{\mu\mu}$ is the resistivity of mass transfer between the surface and the liquid and $R^{s,v}_{\mu\mu}$ is the resistivity of mass transfer between the surface and the vapor phase. Applying simplifying assumptions and the

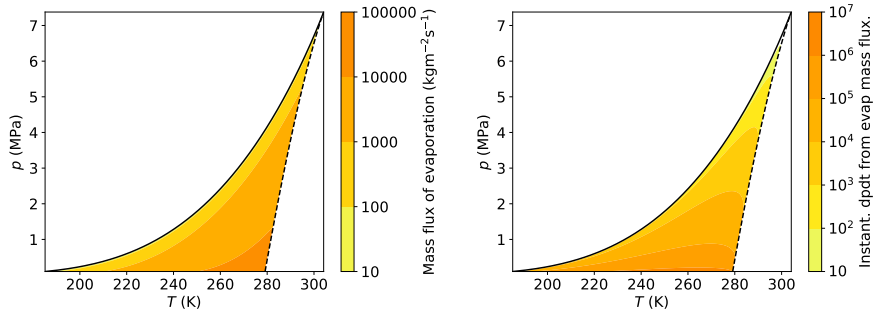

(a) Estimated evaporation mass flux through a liquid-vapor interface based on Equations (24) and (25).

(b) Rate of change in pressure for a closed volume with the evaporation mass flux shown in Fig (a), assuming that $T_\ell = T_v$ and $p_\ell = p_v$.

Figure 8: Calculated evaporation mass flux (a) and the resulting rate of change in pressure in a closed system (b) shown in the CO_2 phase diagram.

kinetic theory of gases, the sum of the resistivities can be approximated as (Kjelstrup and Bedeaux, 2008)

$$R^{s,\ell}_{\mu\mu} + R^{s,v}_{\mu\mu} = \frac{2k_B}{u_{\mathrm{mp}}(T^s)\rho_v^{\mathrm{sat}}(T^s)m}\left(\alpha^{-1} + \frac{1}{5\pi} - \frac{31}{32}\right), \tag{25}$$

where T^s is the temperature of the interface, $u_{\mathrm{mp}}(T^s) = \sqrt{2k_BT^s/\pi m}$ is the most probable thermal velocity, $\rho_v^{\mathrm{sat}}(T^s)$ is the density of saturated vapor at the surface between liquid and vapor and α is the condensation coefficient approximating the fraction of incident particles which are absorbed by the liquid surface after collision. In the present work, we take $T^s = T$ due to the temperature equilibrium condition of the pipe flow model. We further assume that $\alpha = 0.5$, i.e., that half of the incident particles on the liquid surface will pass through it.

In Figure 8a, we show how the mass flux predicted by this evaporation model varies for different regions in the phase diagram. For a closed system with a volume of 1 m^3, a surface area of 1 m^2, and the thermodynamic constraints of our flow model ($T_\ell = T_v$, $p_\ell = p_v$), the resulting rate of change in pressure caused by the predicted evaporation mass flux is illustrated in Figure 8b. We note that these plots seem to better agree with the maximum superheat observed for colder temperatures in depressurization experiments.

3.4. Interfacial area density

In order to determine the total mass-transfer rate caused by evaporation at the bubble surface, the interfacial area density between liquid and vapor must be determined, cf. Equation (24). Similarly to the approach described by Pinhasi *et al.* (2005), our estimates depend on assumed flow regimes based on the volume fraction of vapor in the flow.

We assume that the bubbles stay separate up until $\alpha_v = 0.3$. With the assumption that the bubbles are perfectly spherical, we can then apply the transport equation for the number density of bubbles to estimate the interfacial area density in the flow.

At volume fractions of $0.3 \leq \alpha_v \leq 0.7$, it is assumed that the bubbles will coalesce and break apart. For simplicity, we generally assume that the coalescence and breakup of bubbles keeps the total interfacial area density conserved. We then apply the

transport equation (13) for the interfacial area density with $S_a = 0$ to find $a_{\text{int,cons}}$. However, if we are approaching conditions where bubble breakup should dominate, we calculate the surface area density based on the number density of bubbles after break up has occurred. The model for bubble breakup is provided in the next section.

At $\alpha_v = 0.7$, we assume that the flow has transitioned to droplet flow. As we lack a model to predict the number of droplets that will be present at this stage, the interfacial area density is currently modeled with a simple correlation to ensure that a_{int} vanishes for single-phase flow when $\alpha_v = 1$.

Our estimate can be summarized as follows for different volume fractions of vapor:

$$a_{\text{int}} = \begin{cases} (36\pi n_b)^{1/3}\alpha_v^{2/3} & \text{if } 0 \leq \alpha_v \leq 0.3 \text{ or } \Delta n_{\text{bub,break}} > 0 \text{ and } \alpha_v \leq 0.7 \\ a_{\text{int,cons}} & \text{if } 0.3 < \alpha_v \leq 0.7 \\ \dfrac{a_{\text{int,cons}}}{0.3}(1-\alpha_v) & \text{if } 0.7 < \alpha_v \leq 1 \end{cases}, \tag{26}$$

where the subscript "cons" denotes that the interfacial area density is taken from the interfacial area conservation and $\Delta n_{\text{bub,break}}$ denotes the change in bubble number density due to bubble breakup as described in the following section.

3.5. Bubble breakup

We model the bubble breakup process inspired by the approach outlined by Ivashnyov *et al.* (2000). It is assumed that bubble breakup will occur once a critical Weber number is approached. We estimate the Weber number based on the expression of Levich (1962) as suggested by Hesketh *et al.* (1987) for the application on turbulent flow in horizontal pipes:

$$We = \left[\frac{2r}{1.38} \frac{\rho_\ell^{0.3}\rho_v^{0.3}\eta_\ell^{0.1}}{\sigma^{0.6}} \frac{|u_\ell|^{1.1}}{D_{\text{pipe}}^{0.5}} \right]^{1/0.6}, \tag{27}$$

where r is the bubble radius, η_ℓ is the dynamic viscosity of the liquid phase and D_{pipe} is the inner diameter of the pipe. To avoid division by zero at the critical point, we limit the surface tension such that $\sigma \approx \sigma(0.95T_{\text{crit}})$ if $T > 0.95T_{\text{crit}}$. The current radius of the bubbles is calculated using the volume fraction and number density of bubbles:

$$r = \left(\frac{3}{4\pi} \frac{\alpha_v}{n_{\text{bub}}} \right)^{1/3}, \tag{28}$$

where we have assumed that the bubbles are spherical.

We assume that the maximum possible bubble radius is the one where the critical Weber number is reached:

$$r_{\text{max}} = \frac{1.38We_{\text{crit}}^{0.6}}{2} \frac{\sigma^{0.6}}{\rho_\ell^{0.3}\rho_v^{0.2}\nu_\ell^{0.1}} \frac{D_{\text{pipe}}^{0.5}}{|u_\ell|^{1.1}}. \tag{29}$$

r_{max} then defines the minimum, or critical, number of bubbles in the flow:

$$n_{\text{crit,break}} = \frac{\alpha_v}{\frac{4}{3}\pi r_{\text{max}}^3}. \tag{30}$$

In Ivashnyov *et al.* (2000), if the Weber number in the flow is found to be greater than the critical Weber number, the corresponding minimum number density of bubbles is

enforced in the flow. Here, we instead apply a logistic function which continuously increases from the present number of bubbles to the critical number of bubbles as a function of the Weber number.

$$\Delta n_{\text{bub,break}} = \frac{n_{\text{crit, break}} - n_{\text{bub}}}{1 + \exp\left(-k\left(We - We_{\text{crit}}\right)\right)} \tag{31}$$

where k is the growth rate of the function. We find that setting $k = 30$ and $We_{\text{crit}} = 2.1$ works reasonably well for our test cases. We limit the calculated radius to be smaller than or equal to $r = 10^{-5}$ m. The choice of this threshold radius is connected to the choice of the critical Weber number and can therefore not be considered an independent parameter.

For the pipe depressurization cases studied in the present work, the resulting pressure near the open end of the pipe is very sensitive to the choice of the critical Weber number. There is no guarantee that the present model will extend to other test cases nor to longer time-frames for the cases that are considered in the present study. The main role of the bubble breakup model is to elevate the pressure near the open end of the pipe over time, accounting for a pressure hump effect observed in experiments (Log *et al.*, 2024; Ivashnyov *et al.*, 2000). We expect the sensitivity to the critical Weber number to reduce for more refined models, e.g., allowing for a temperature difference in the phases such that heat-transfer governed bubble growth can be applied.

3.6. Summary

This section provides a concise overview of the relevant equations for the mass-transfer model in the HFM. The mass-transfer rate in the HFM consists of the sum of contributions from homogeneous nucleation, heterogeneous nucleation and bubble growth through evaporation:

$$\Gamma = \Gamma_{\text{hom}} + \Gamma_{\text{het}} + \Gamma_{\text{evap}}, \tag{32}$$

where Γ_{hom} is calculated using CNT and is given by Equation (21), $\Gamma_{\text{het}} = K_m$ where K_m is a constant chosen to fit experimental data and $\dfrac{\Gamma_{\text{evap}}}{a_{\text{int}}}$ is estimated using Equation (24).

To determine the mass transfer due to evaporation, Γ_{evap}, we must estimate the interfacial area density between the liquid and vapor phases, a_{int}. The interfacial area density a_{int} is approximated by Equation (26), where different flow regimes are assumed based on the volume fraction of vapor.

When $\alpha_v < 0.3$, or $\alpha_v < 0.7$ and bubble breakup is found to dominate, a_{int} is estimated based on the bubble number density in the flow. The bubble source term in the transport equation (12) for bubbles, J_{bub}, is modeled by

$$J_{\text{bub}} = J_{\text{hom}} + J_{\text{het}} + J_{\text{break}} + J_{\text{coal}}, \tag{33}$$

where J_{hom} is calculated using CNT and is given by Equation (17) and $J_{\text{het}} = K_b$ where K_b is a constant fitted to experimental data. The bubble number density added due to bubble breakup is described in Section 3.5. Provided that bubble breakup is not dominating the flow, coalescence of bubbles is emulated by enforcing the conservation of interfacial area density for $0.3 \leq \alpha_v \leq 0.7$. Finally, for $\alpha_v > 0.7$ a simple function is applied to ensure that $a_{\text{int}} \to 0$ as $\alpha_v \to 1$.

4. Numerical methods

4.1. Numerical discretization

We now consider the numerical solution of the HFM. The governing equations, (5)–(8) with the additional flow topology equations (12)–(13), can be written in the vectorial form

$$\frac{\partial \boldsymbol{U}}{\partial t} + \frac{\partial \boldsymbol{F}}{\partial x} = \boldsymbol{S}, \tag{34}$$

where

$$\boldsymbol{U} = \begin{pmatrix} \alpha_v \rho_v \\ \alpha_\ell \rho_\ell \\ \rho u \\ E \\ n_{\text{bub}} \\ a_{\text{int}} \end{pmatrix}, \ \boldsymbol{F}(\boldsymbol{U}) = \begin{pmatrix} \alpha_v \rho_v u \\ \alpha_\ell \rho_\ell u \\ \rho u^2 + p \\ (E + p)u \\ n_{\text{bub}} u \\ a_{\text{int}} u \end{pmatrix}, \ \boldsymbol{S} = \begin{pmatrix} \Gamma \\ -\Gamma \\ \rho g_x - \mathcal{F} \\ \mathcal{Q} \\ J_{\text{bub}} \\ S_a \end{pmatrix},$$

and where we include both the bubble transport equation and the transport equation for interfacial area density. Depending on the resulting local volume fraction, the rate of change of interfacial area, S_a, is set to zero or determined based on the bubble transport equation, in consistency with Section 3.4. The flow topology equations are linearly independent and contribute to the eigenstructure of the system with two characteristic waves overlapping the contact discontinuity, having eigenvalues of u.

The system (34) is solved using a classical first-order fractional step method known as Godunov splitting (LeVeque, 2002, Ch. 17). In Godunov splitting, two steps are applied to reach the solution. First, the homogeneous part of the system is solved without the source term,

$$\frac{\partial \boldsymbol{U}}{\partial t} + \frac{\partial \boldsymbol{F}}{\partial x} = \boldsymbol{0}. \tag{35}$$

The solution of the first step is then applied in the second relaxation step, where the following ODE is solved

$$\frac{\mathrm{d}\boldsymbol{U}}{\mathrm{d}t} = \boldsymbol{S}(\boldsymbol{U}). \tag{36}$$

The homogeneous part of the system is solved using the Harten–Lax–van Leer-Contact (HLLC) finite-volume method (FVM) (Toro *et al.*, 1994) in space and the explicit Euler method in time. Details on the HLLC FVM for the HRM* can be found in Log *et al.* (2024). The transport equations for the bubble number density and the interfacial area density are discretized equivalently to the mass balance equations in Log *et al.* (2024). Finally, the ODE (36) is solved with the implicit Euler method using Newton-Raphson iterations. The ODE is solved simultaneously with the thermodynamic variables, as described in the following section.

At the open end of the pipe, a Bernoulli-choking-pressure boundary condition (BBC) is applied using a single ghost cell outside the computational domain of the pipe. Details on the BBC for the HRM* can be found in Log *et al.* (2024), and the method is equivalent for the HFM. Briefly summarized, the flow velocity, entropy and mass fraction are extrapolated from the first cell in the computational domain and the pressure in the ghost cell is set as the approximate choking pressure based on a steady flow assumption. If the liquid spinodal is reached along the flow isentrope, the minimum amount of vapor required to keep the liquid stable is added to avoid issues with the thermodynamic calculations. The assumption of frozen or minimal flashing ensures that the pressure set in the ghost cell is always equal to or lower than the pressure in the computational domain. Thus, the BC cannot restrict the predicted pressure undershoot or superheat in the computational domain.

4.2. Evaluation of the thermodynamic state and mass transfer in each grid cell

The thermodynamic state and mass transfer is evaluated in each grid cell in the domain to satisfy the governing equations of the flow. After the conservative part of the flow equations is solved using the HLLC FVM, the resulting conserved variables will be known in each grid cell: $(\alpha_v\rho_v)_{\text{spec}}$, $(\alpha_\ell\rho_\ell)_{\text{spec}}$, $(\rho u)_{\text{spec}}$, E_{spec}, $n_{\text{bub, spec}}$ and $a_{\text{int, spec}}$, where the subscript spec denotes *specified* variables. Based on the known variables, the total density of the fluid in the given grid cell is

$$\rho_{\text{spec}} = (\alpha_v\rho_v)_{\text{spec}} + (\alpha_\ell\rho_\ell)_{\text{spec}}, \tag{37}$$

the velocity of the flow is

$$u_{\text{spec}} = \frac{(\rho u)_{\text{spec}}}{\rho_{\text{spec}}} \tag{38}$$

and the internal energy of the mixture becomes

$$(\rho e)_{\text{spec}} = E_{\text{spec}} - \frac{1}{2}\rho_{\text{spec}}u^2_{\text{spec}}. \tag{39}$$

In order to define the thermodynamic state of the two phases in the HFM, four thermodynamic variables are needed. We choose to solve for α_v, ρ_v, ρ_ℓ and T. Additionally, we solve for the number of bubbles in the flow. These variables must satisfy the mass balances for the two phases, the conservation of internal energy during the mass-transfer process, the equality of pressures for the two phases and the balance of bubbles:

$$\boldsymbol{f} = \begin{pmatrix} \alpha_v\rho_v - \left((\alpha_v\rho_v)_{\text{spec}} + \Delta m_v\right) \\ (1-\alpha_v)\rho_\ell - \left((\alpha_\ell\rho_\ell)_{\text{spec}} + \Delta m_\ell\right) \\ \alpha_v\rho_v e_v(\rho_v, T) + (1-\alpha_v)\rho_\ell e_\ell(\rho_\ell, T) - (\rho e)_{\text{spec}} \\ p_v(\rho_v, T) - p_\ell(\rho_\ell, T) \\ n_{\text{bub}} - \left(n_{\text{bub,spec}} + \Delta n_{\text{bub}}\right) \end{pmatrix} = \mathbf{0}, \tag{40}$$

where Δm_v denotes the mass transfer from liquid to vapor during the time step Δt,

$$\Delta m_v = -\Delta m_\ell = \int_t^{t+\Delta t} \Gamma dt. \tag{41}$$

We presently apply a simple Euler step in the time integration:

$$\Delta m_v \approx \Gamma \Delta t. \tag{42}$$

Similarly, Δn_{bub} denotes the nucleation of bubbles during this time step:

$$\Delta n_{\text{bub}} = (J_{\text{hom}} + J_{\text{het}})\Delta t. \tag{43}$$

Note that $\Delta m_v = \Delta m_v(\alpha_v, \rho_v, \rho_\ell, T)$ and $\Delta n_{\text{bub}} = \Delta n_{\text{bub}}(\alpha_v, \rho_v, \rho_\ell, T)$, i.e., the mass-transfer term Γ and bubble creation rates $J_{\text{hom}}, J_{\text{het}}$ are functions of the solution state. The method is therefore implicit, so the mass transfer is solved using the implicit Euler method. Note that the complete two-step solution procedure with the HLLC FVM and the subsequent implicit solution of the ODE (36) using Equation (40) ensures mixture-energy-consistency as defined by Pelanti and Shyue (2014).

The set of equations (40) can be solved by an iterative method. In the present work, we apply a Newton-Raphson solver. For numerical reasons we found it best to add the

Table 1: Initial conditions of the full-bore CO_2 depressurization tests.

Test no.	Pressure avg. (MPa)	Temperature avg. (°C)	Ambient temp. (°C)
4[**]	12.54	21.1	22
6[**]	10.40	40.0	6
8[**]	12.22	24.6	9
19[*]	12.47	10.2	18
22[*]	12.48	14.9	14
23[*]	12.19	31.5	15
24[*]	11.56	35.8	10
25[†]	12.27	4.6	-8.5

[**] Munkejord *et al.* (2020a), [*] Log *et al.* (2024), [†] present work.

contribution of bubble breakup directly in the calculation of the interfacial area density during the iteration process. The contribution of bubble breakup is therefore always included in the mass-transfer calculation, but the number of bubbles is only updated with the bubbles generated due to breakup after the iterations have converged.

In certain areas of the phase diagram, CNT predicts extremely small values for the rate of bubbles and mass being added to the flow. In order to avoid numerical issues with vanishingly small masses and numbers of bubbles being produced, we enforce the following threshold: If the iterations converge to a solution with $\alpha_v \rho_v < 10^{-100}$, we set $\rho_\ell = \rho_{\text{spec}}$, $n_{\text{bub}} = 0$ and $\alpha_v = 0$.

5. Results and discussion

In this section, we briefly introduce the experimental data used to fit the parameters for heterogeneous nucleation in the HFM in Section 5.1 and evaluate the model fit in Section 5.2. We then compare the modeled pressure estimates to experimental values for different initial conditions with very different flashing characteristics in Section 5.3. Finally, we investigate the contributions of the homogeneous and heterogeneous bubble nucleation models of the HFM in more detail in Section 5.4.

5.1. Depressurization experiments

To show the range of applicability of the present model, we compare calculations with data from the ECCSEL depressurization facility (ECCSEL, 2021). The test section consists of a 61.67 m long pipe with an inner diameter of 40.8 mm. The pipe is densely instrumented with high-frequency pressure and temperature sensors. The pressure measurements are logged at 100 kHz and the measurement uncertainty has been estimated to be 60 kPa with a 95% confidence level. Details on the experimental setup, procedure and equipment, including the heat transfer properties of the test section and surface roughness of the pipe can be found in Munkejord *et al.* (2020a).

As discussed in further detail by Log *et al.* (2024), a series of full-bore depressurization tests with pure CO_2 have been conducted at this facility for a range of initial temperatures. The data from these experiments are available at Zenodo (Munkejord *et al.*, 2020b; Log *et al.*, 2023a). The initial conditions for these tests, including one new test (Test 25), are presented in Table 1. Test 25 is the coldest test conducted at the facility to date and its results are first presented here. The data from this experiment is available at Log *et al.* (2023b).

We show the depressurization paths of the warmest (Test 6), coldest (Test 25) and the intermediate-temperature test (Test 4) in the CO_2 phase diagram in Figure 9. We

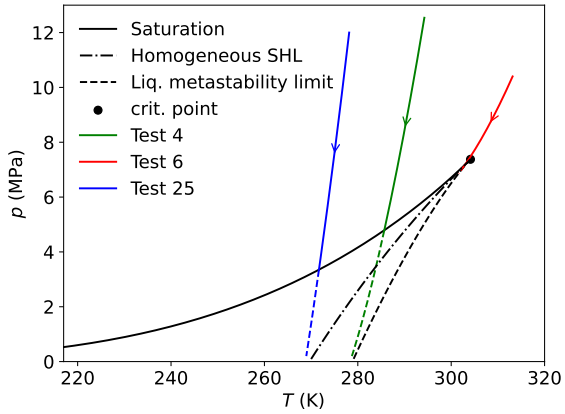

Figure 9: Calculated single-phase isentropic depressurization paths of the warmest (Test 6), coldest (Test 25) and an intermediate temperature (Test 4) depressurization test conducted at the ECCSEL depressurization facility. The dashed part of the depressurization paths illustrate the possible metastable path before flashing begins.

also show the homogeneous superheat limit ($J_{\text{hom}}(T) = 10^{12}$ bubbles m^{-3} s^{-1}) in the phase diagram. The warmest test has a depressurization path which crosses the saturation curve at a temperature 1.2 K below the critical temperature. The intermediate-temperature experiment crosses the saturation curve at a temperature 18.5 K below the critical temperature while that temperature difference is 32.5 K for the coldest experiment. As shown in Figure 9, the depressurization path of the coldest test, Test 25, does not cross the superheat limit estimated from homogeneous nucleation, so this test is only affected by heterogeneous nucleation.

5.2. Choice of coefficients in the heterogeneous nucleation model

In this section, we demonstrate how the choice of the mass-transfer rate (K_m) and bubble nucleation rate (K_b) modeling heterogeneous nucleation (23) affects the resulting depressurization wave inside the pipe. This investigation was done for all the full-bore depressurization tests reported in Table 1, with similar results for all the tests. In the following, we take Test 4 as an example to be discussed in detail. We model the flow in 15 m of the pipe using $N = 250$ grid cells. The grid was found to be sufficiently fine while providing a low computational time for model fitting.

In Figure 10a we show the resulting pressure profile in the pipe at $t = 20$ ms when we vary K_b while keeping $K_m = 400$ kg m^{-3} s^{-1} constant. When $K_b = 0$ we get a linear increase in pressure from the pipe outlet until the equilibrium pressure is reached approximately 4 m inside the pipe. When the bubble nucleation rate is increased, the pressure rises faster near the outlet, creating a more curved pressure profile in the region before the equilibrium pressure is met, 4 m inside the pipe. For higher bubble nucleation rates, the pressure profile approaches the profile predicted by the HEM.

In Figure 10b, we show the resulting pressure profile in the pipe at $t = 20$ ms when we vary K_m while keeping $K_b = 10$ bubbles m^{-3} s^{-1} constant. Varying K_m affects the resulting pressure level. For $K_m = 100$ kg m^{-3} s^{-1}, the pressure remains lower than the equilibrium pressure in the region behind the single-phase portion of the depressurization wave, i.e., for $x < 7.5$ m. For $K_m = 400$ kg m^{-3} s^{-1}, the equilibrium pressure is met

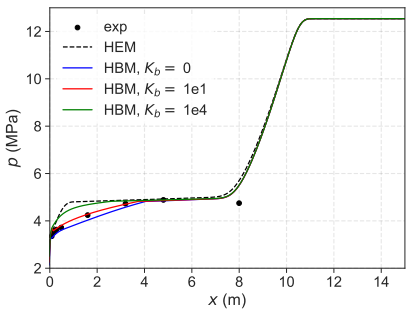

(a) Pressure profile along the pipe for varying heterogeneous bubble nucleation rates, K_b and a constant mass-transfer rate, $K_m = 400\,\mathrm{kg\,m^{-3}\,s^{-1}}$.

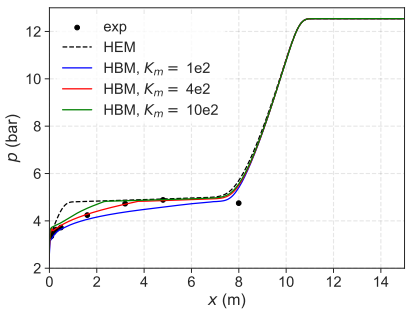

(b) Pressure profile along the pipe for varying heterogeneous mass-transfer rates, K_m, with a constant bubble nucleation rate, $K_b = 10$ bubbles $\mathrm{m^{-3}\,s^{-1}}$.

Figure 10: Investigation of the effect of varying the bubble formation rate and the mass-transfer rate caused by heterogeneous nucleation for Test 4 (with initial conditions given in Table 1). The results are plotted at time $t = 20$ ms.

Table 2: The mean absolute percentage error for the model fit of the HRM* and HFM pressure predictions to the experimental measurements at 8 cm, 28 cm, 48.4 cm and 1.6 m from the open end of the pipe over $t = 20$ ms after disk rupture.

Test no.	Temperature avg. (°C)	MAPE HRM* (%)	MAPE HFM (%)
6	40.0	2.2	1.7
24	35.8	4.2	3.2
23	31.5	7.4	5.8
8	24.6	7.8	6.3
4	21.1	8.3	3.5
22	14.9	12.7	6.8
19	10.2	7.6	9.0
25	4.6	10.8	11.5

around 4 m inside the pipe, and for $K_m = 1000\,\mathrm{kg\,m^{-3}\,s^{-1}}$ the equilibrium pressure is met around 2.5 m inside the pipe.

The parameter values for K_b and K_m were fitted by visual inspection to capture the recorded pressure profile at $t = 20$ ms and the recorded pressure traces for the first 20 ms of the depressurization, for all of the experiments listed in Table 1. We found that applying $K_b = 10$ bubbles $\mathrm{m^{-3}\,s^{-1}}$ and $K_m = 400\,\mathrm{kg\,m^{-3}\,s^{-1}}$ gave the best agreement with the experimental results for all cases. The resulting pressure profiles for the remaining depressurization tests conducted at different initial conditions are shown in Figure 11, and Figures 13 and 18.

We now assess and compare the model fit of the HRM* and HFM models to the experimental data using the average mean absolute percentage error (MAPE) at four sensor locations close to the open end of the pipe over the first $t = 20$ ms after the disk rupture at 0.1 ms intervals. For these simulations, a fine grid was applied with $N = 2500$ cells. The sensor locations were 8 cm, 28 cm, 48.4 cm and 1.6 m from the open end of the pipe, and the result is reported in Table 2. The average MAPE was 7.6% for the HRM* and 6.0% for the HFM. The HFM gave a lower MAPE for all tests, except the two coldest ones. The mass transfer for the HRM* is determined by the relaxation time which varies significantly for each depressurization case using the correlation (10) to fit the data (Log *et al.*, 2024). The HFM achieved a similar accuracy

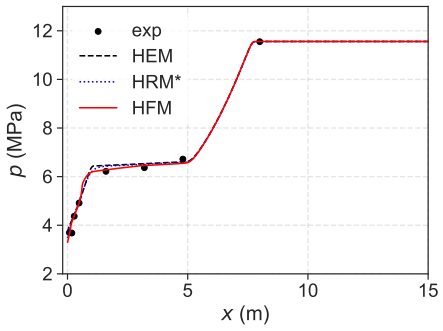

(a) Test 24: $p_0 = 11.6\,\text{MPa}$, $T_0 = 35.8\,^\circ\text{C}$

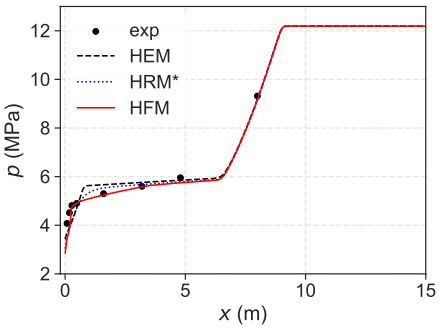

(b) Test 23: $p_0 = 12.2\,\text{MPa}$, $T_0 = 31.5\,^\circ\text{C}$

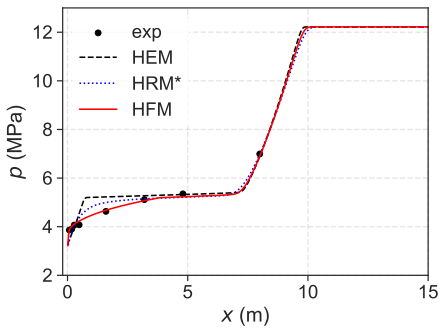

(c) Test 8: $p_0 = 12.2\,\text{MPa}$, $T_0 = 24.6\,^\circ\text{C}$

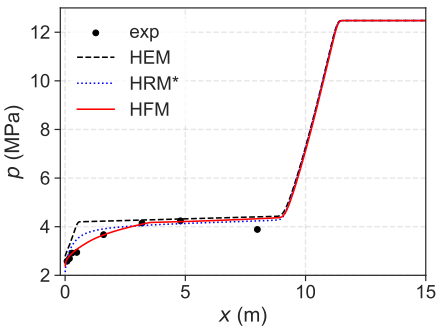

(d) Test 22: $p_0 = 12.5\,\text{MPa}$, $T_0 = 14.9\,^\circ\text{C}$

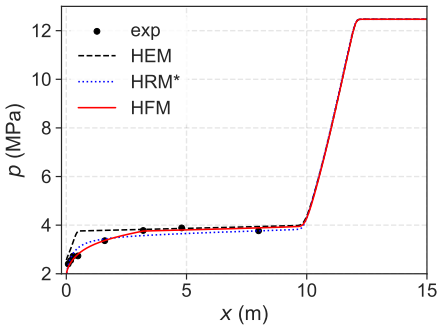

(e) Test 19: $p_0 = 12.5\,\text{MPa}$, $T_0 = 10.2\,^\circ\text{C}$

Figure 11: Comparison of experimentally measured and modeled pressure profiles along the pipe at $t = 20\,\text{ms}$ for depressurization tests conducted at various initial temperatures. For the HFM, setting the parameters for heterogeneous nucleation to $K_b = 10$ bubbles $\text{m}^{-3}\,\text{s}^{-1}$ and $K_m = 400\,\text{kg}\,\text{m}^{-3}\,\text{s}^{-1}$ worked well for all the tests.

while applying constant parameter values. This supports our hypothesis that including homogeneous nucleation in flashing flow models improves their predictive ability.

5.2.1. A note on the chosen value for K_b

The fitted value of the heterogeneous bubble nucleation rate, K_b, in the HFM suggests that only 10 bubbles nucleate heterogeneously in one cubic meter of CO_2 per second. This number is very low, and likely not physical. In practice, such a low value of K_b leads to a limited surface area for evaporation to occur, thus limiting the evaporation/bubble growth in the model. Therefore, the present bubble growth model described in Section 3.3 may be too strong, for the following reasons:

- One of the model assumptions for the bubble growth is that the evaporation occurs through a stationary surface. However, there is a limited quantity of liquid available to be supplied towards the liquid–vapor interface and evaporate at any given moment to keep the surface stationary. The process is instead likely limited by the heat transfer between the bubble and the surrounding liquid, and/or the wall of the pipe.

- The present model assumes that the process of bubble growth is driven by a difference in chemical potentials between the phases. Our flow model further assumes equal temperatures and pressures of the phases. This causes a thermodynamic state of the liquid–vapor mixture which may exaggerate the difference in chemical potentials between the phases, causing a too high driving force for bubble growth.

- The present formulation of the resistivities in the bubble growth model is based on kinetic gas theory and several simplifying assumptions and relations which may not be representative in the relevant area of the phase diagram. Furthermore, the accommodation coefficient for evaporation through the surface of the bubble is unknown and may not be constant.

Based on the limitations of the bubble growth (and flow) model currently applied, it may be advantageous to test the HFM mass-transfer terms for a flow model which allows the phases to be at different temperatures, and apply a bubble growth model driven by heat transfer, such as the ones in Shin and Jones (1993); Blinkov *et al.* (1993); Ivashnyov *et al.* (2000) and Liao and Lucas (2017a).

5.3. Comparison to experimental measurements

We now study in more detail how the flow models presented in Section 2 fit the experimental measurements for the warm (Test 6), intermediate temperature (Test 4) and cold (Test 25) pipe depressurization experiments. For all the tests, we model 15 m of the pipe using a fine grid with $N = 2500$ grid cells and applying a CFL number of 0.9. The simulations end at $t_{\text{end}} = 20$ ms. For the heterogeneous nucleation in the HFM, we set $K_b = 10$ bubbles $\text{m}^{-3}\,\text{s}^{-1}$ and $K_m = 400\,\text{kg}\,\text{m}^{-3}\,\text{s}^{-1}$ for all cases, as discussed in the previous section. For the HRM*, the relaxation time is found using the correlation (10), which gave $\theta = 0.04$ ms for Test 6, $\theta = 1.50$ ms for Test 4 and $\theta = 2.82$ ms for Test 25.

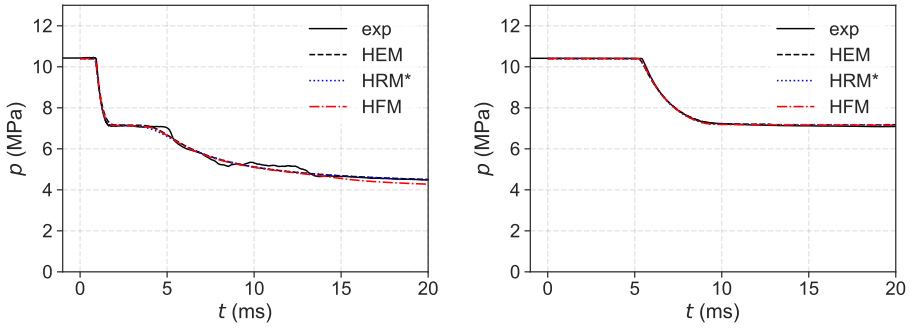

(a) 28 cm from open end.

(b) 160 cm from open end.

Figure 12: Comparison of experimentally measured pressure at $x = 28\,\text{cm}$ and $x = 160\,\text{cm}$ from open end with model predictions of the HEM, HRM* and the HFM for the warm depressurization test, Test 6.

5.3.1. Test 6 — warmest case

In Figure 12, we show the experimental and modeled pressure traces for Test 6 at the positions $x = 28\,\text{cm}$ and $x = 160\,\text{cm}$ from the open end of the pipe. We compare the results to the HEM and the HRM*. As discussed in detail in Log *et al.* (2024), nearly no non-equilibrium effects are present for this test due to the depressurization path crossing the saturation curve so close to the critical point of CO_2. The HEM's predicted pressure is in excellent agreement with the recorded pressure trace, both at $x = 28\,\text{cm}$ as shown in Figure 12a and $x = 160\,\text{cm}$ as shown in Figure 12b. The HRM* pressure overlaps with that of HEM, as it is explicitly fitted with a short relaxation time. The HFM pressure prediction mostly overlaps with that of HEM and is also in excellent agreement with the recorded pressure traces. After $t = 10\,\text{ms}$, the HFM predicts a few bar lower pressure than the recorded pressure at $x = 28\,\text{cm}$ from the open end of the pipe.

Note that the HEM and HRM* predictions for this case are forced to be at or close to equilibrium. This is not the case for the HFM. The near-equilibrium result of the HFM is due to the accurate flashing model and in particular the homogeneous nucleation term, which is very strong near the critical point. Also note that for the present case, a small error in the numerical solution procedure can bring the liquid phase into its thermodynamically unstable region, causing thermodynamic solution routines to fail. Thus, the present case demonstrates the robustness of the numerical solution method for the HRM* and HFM as well.

We further compare the model predictions with the recorded pressure profile along the pipe at $t = 20\,\text{ms}$ as shown in Figure 13. In Figure 13a we show the measured and modeled pressure profile along 15 m of the pipe. As observed earlier, the pressure predictions of both HEM and HRM* agree well with the experimental recordings. The HFM provides nearly overlapping predictions with the HEM, with the exception of a somewhat lower predicted pressure near the open end of the pipe. This can be seen more easily in Figure 13b, where we have zoomed in on the pressure plateau and the slow-moving part of the depressurization wave in the two-phase mixture. We note that a similar trend is observed in the experimental data near the open end. The lower pressure occurs in a region where the HFM predicts $\alpha_v > 0.7$.

For $\alpha_v > 0.7$, we assume that the interfacial area between liquid and vapor starts to decrease, cf. Equation (26) which gives an exponential decrease in the interfacial area density. For $\alpha_v = 0.74$, at $x = 0.455\,\text{m}$ the interfacial area has reduced significantly

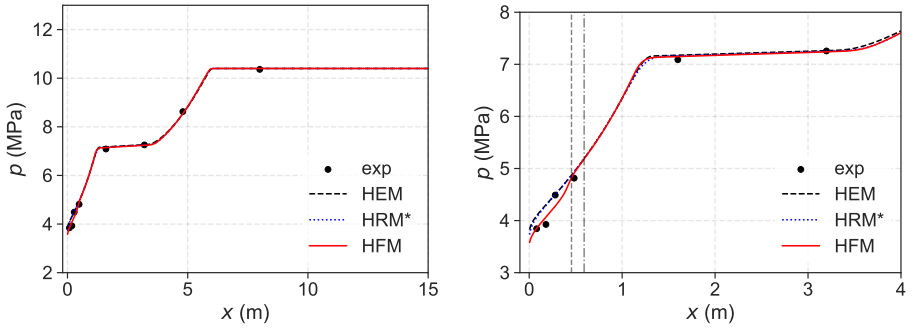

(a) $t = 20$ ms

(b) $t = 20$ ms (zoomed). The vertical lines indicate the points where $\alpha_g = 0.7$ (dash dotted) and $\alpha_g = 0.74$ (dashed).

Figure 13: Comparison of experimentally measured pressure along the pipe with model predictions of the HEM, HRM* and the HFM for the warm depressurization test, Test 6.

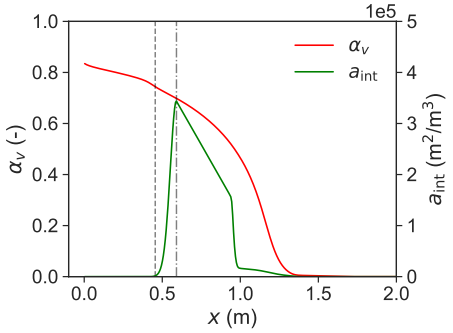

Figure 14: HFM prediction of volume fraction (red, left y axis) and interfacial area density (green, right y axis) along the pipe for the warm depressurization test, Test 6. The vertical lines indicate the points where $\alpha_g = 0.7$ (dash dotted) and $\alpha_g = 0.74$ (dashed). $t = 20$ ms.

enough that evaporation/bubble growth cannot keep the pressure elevated to the saturation pressure. The volume fraction and estimated interfacial area density along the pipe are shown in Figure 14. The experimental data is consistent with a reduction in the interfacial area density near the open end, though it seems to occur slightly closer to the open end than what is predicted by the HFM.

5.3.2. Test 4 — Intermediate-temperature case

In Figure 15, we show the experimental and modeled pressure traces for Test 4 at the positions $x = 28$ cm and $x = 160$ cm from the open end of the pipe. For this test, the recorded pressure traces and pressure prediction of the non-equilibrium models clearly deviate from the pressure modeled by HEM. The HEM overpredicts the pressure, especially for the first 10 ms near the open end of the pipe, as shown in Figure 15a. Further inside the pipe, the HEM pressure prediction is still too high, but the deviation is smaller. The HFM pressure agrees well with the recorded pressure traces, both at $x = 28$ cm and $x = 160$ cm, though the model fails to capture an increased pressure undershoot occurring at $x = 28$ cm for t =2.5 ms to 5 ms. At $x = 160$ cm, the HFM pressure overlaps nearly perfectly with the recorded pressure. In this region the HRM* slightly overpredicts the pressure.

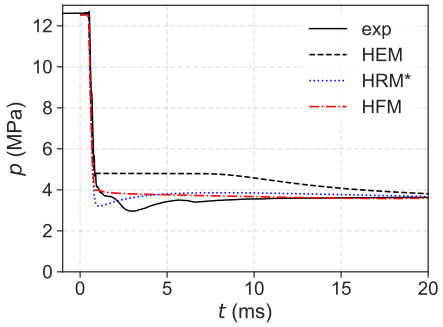

(a) 28 cm from open end.

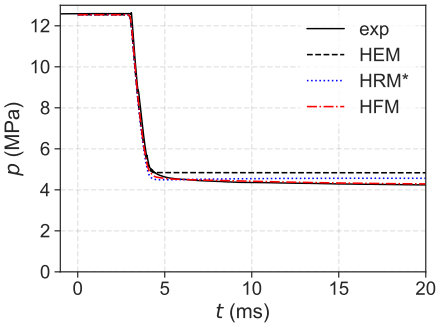

(b) 160 cm from open end.

Figure 15: Comparison of experimentally measured pressure at $x = 28$ cm and $x = 160$ cm from open end with model predictions of the HEM, HRM* and the HFM for the intermediate-temperature depressurization test, Test 4.

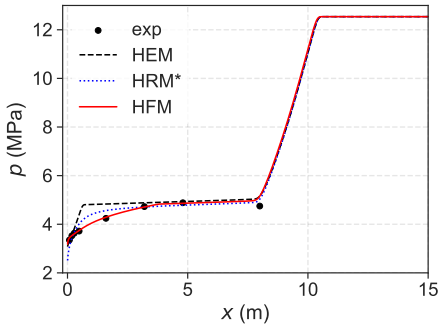

(a) $t = 20$ ms

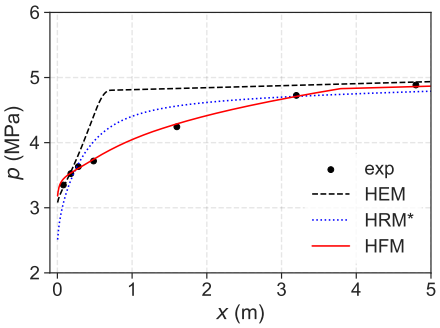

(b) $t = 20$ ms (zoomed)

Figure 16: Comparison of experimentally measured pressure along the pipe with model predictions of the HEM, HRM* and the HFM for the intermediate-temperature depressurization test, Test 4.

In Figure 16, we compare model predictions with the recorded pressure profile along the pipe at $t = 20$ ms. As shown in Figure 16a, the HEM overpredicts the pressure near the open end for $x < 4$ m, and gives a too slow-moving two-phase wave. The HRM* predicts a too low pressure at the pipe outlet and then predicts a too fast increase in the pressure along the x-axis. The HFM pressure agrees very well with the recorded pressure profile in the pipe. The difference in the pressure predictions of the models is most pronounced near the pipe outlet and can be more clearly seen in Figure 16b, where we zoom in on the first 5 m of the pipe. The elevated pressure near the open end for HFM is caused by the bubble breakup model. The bubble breakup provides extra available interfacial area for bubble growth, enhancing the flashing. This is in agreement with the results of Ivashnyov *et al.* (2000).

5.3.3. Test 25 — coldest case

In Figure 17, we show the experimental and modeled pressure traces for Test 25 at the positions $x = 28$ cm and $x = 160$ cm from the open end of the pipe. As discussed earlier, this test has such a cold initial condition that only the heterogeneous nucleation term contributes in the HFM. For this test, a triple-layered rupture disk was used. As the different layers did not all open exactly at the same time, we see some jagged pres-

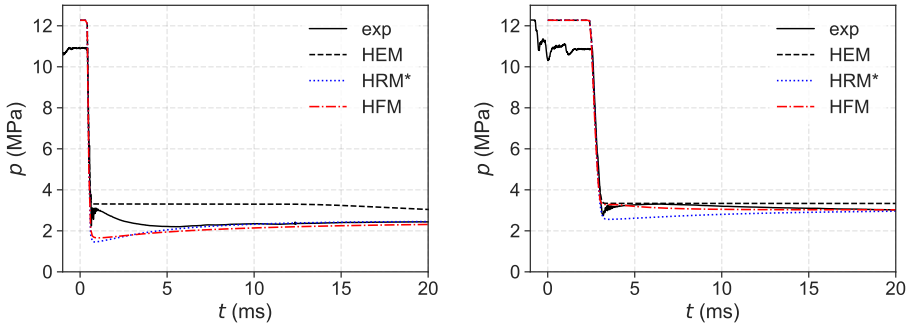

(a) 28 cm from open end.

(b) 160 cm from open end.

Figure 17: Comparison of experimentally measured pressure at $x = 28\,\text{cm}$ and $x = 160\,\text{cm}$ from open end with model predictions of the HEM, HRM* and the HFM for the cold depressurization test, Test 25.

sure traces from the disk opening for $t \leq 3\,\text{ms}$ in Figure 17b. In the fluid simulations, the opening process of the rupture disk was assumed to be instantaneous, causing a discrepancy between the simulated and recorded pressure wave. As this inaccuracy is equal for all the models, their results can still be directly compared.

Similarly to the intermediate-temperature test, the experimentally recorded pressure traces deviate from the HEM for Test 25. This is most evident in Figure 17a, showing the pressure evolution at $x = 28\,\text{cm}$ from the open end of the pipe. Here, the HEM again overestimates the pressure significantly after approximately $t = 2\,\text{ms}$. Both the HRM* and the HFM underpredict the pressure at $x = 28\,\text{cm}$ for the first $t = 5\,\text{ms}$. The recorded pressure trace suggests that chaotic bubble nucleation is occurring just after the fast pressure drop, where we see a series of small pressure oscillations. Due to the simplicity of the model for the heterogeneous nucleation, it is reasonable that this process is not captured well by the HFM. After the initial nucleation process, the recorded pressure remains quite high for the first 3 ms to 4 ms before it falls to a similar level as the pressure predicted by HRM* and HFM. The HRM* and HFM pressure evolutions agree well with the recorded pressure trace for $t > 5\,\text{ms}$, though the pressure of the HFM remains slightly below the experimental measurement. At $x = 160\,\text{cm}$, the recorded pressure agrees fairly well with all the models, though the HFM appears to capture the pressure evolution best.

In Figure 18a, we show the measured and modeled pressure 15 m along the pipe at $t = 20\,\text{ms}$ for Test 25. We observe the same general trends as for the intermediate-temperature test with HEM overpredicting the pressure near the open end and HFM pressure agreeing well with the recorded depressurization wave. However, when we zoom in near the open end of the pipe, we see that the pressure is underpredicted by HFM at positions closer than 0.5 m from the open end. In this region, the mass-transfer rate and bubble nucleation rate should likely be higher than the constant values we have set to model heterogeneous nucleation. The HRM* predicts a similar pressure estimate as the HFM close to the open end. However, further inside the pipe, behind the fast-moving rarefaction wave, the pressure is somewhat underpredicted. This suggests that the relaxation time in the HRM* should be shorter further inside the pipe in order to bring the pressure closer to equilibrium.

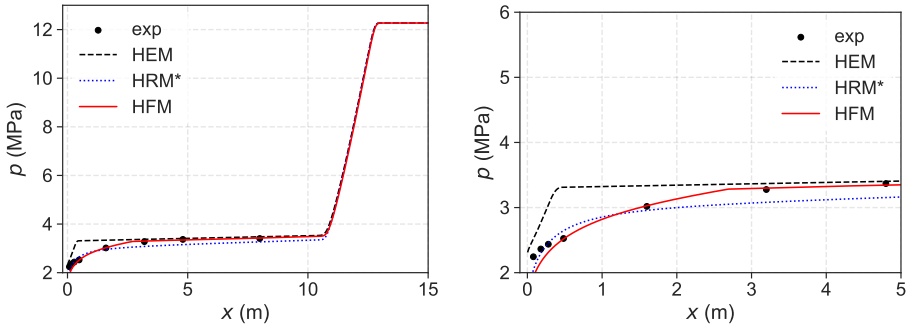

(a) $t = 20$ ms (b) $t = 20$ ms (zoomed)

Figure 18: Comparison of experimentally measured pressure along the pipe with model predictions of the HEM, HRM* and the HFM for the cold depressurization test, Test 25.

5.3.4. Discussion

In the present section, we have tested the HFM against CO_2 depressurization data for three different initial conditions, with very different flash boiling characteristics. For the warmest test with $p_0 = 10.4$ MPa and $T_0 = 40.0\,^{\circ}$C, flashing occurs very close to the critical point. Nearly no metastability occurs before flashing begins and the homogeneous nucleation term is very strong. For the intermediate-temperature test with $p_0 = 12.6$ MPa and $T_0 = 21.1\,^{\circ}$C, there is a significant pressure undershoot before flashing occurs, and both homogeneous and heterogeneous nucleation are present. For the coldest test with $p_0 = 12.3$ MPa and $T_0 = 4.6\,^{\circ}$C, only heterogeneous nucleation contributes to the flashing.

For all the tests, the HFM pressure predictions agree well with the recorded pressure traces, showing the model's capability of capturing the different flashing processes. Note that the same coefficients were used to model the contribution of heterogeneous nucleation in all cases. In contrast, the relaxation time applied in the HRM* to fit the experimental data varies from $\theta = 0.04$ ms for the warmest test to $\theta = 2.82$ ms for the coldest test. The HFM furthermore predicts the pressure profile in the pipe more accurately than the HRM*. We note that for the coldest test, the HFM might benefit from a more refined model for the heterogeneous nucleation as the pressure is underestimated close to the open end of the pipe. Nevertheless, it is clear that by incorporating homogeneous nucleation in the mass-transfer model, the need for model tuning is significantly reduced and the predictive ability of the model is enhanced — which is vital for the application in engineering tools for safety evaluations, where flow estimates for unknown scenarios must be made a priori as data for fitting parameters may not be available.

5.4. Effect of the homogeneous and heterogeneous nucleation terms

In this section, we evaluate the importance and contribution of the heterogeneous and homogeneous nucleation models for the mass-transfer rate in the HFM, see Equation (15). We conduct this study for the intermediate-temperature test case, Test 4, as this case is affected by both homogeneous and heterogeneous nucleation. Furthermore, the depressurization path does not cross the metastability limit so we can safely vary or omit different mass-transfer contributions without reaching the thermodynamically unstable area of the liquid phase.

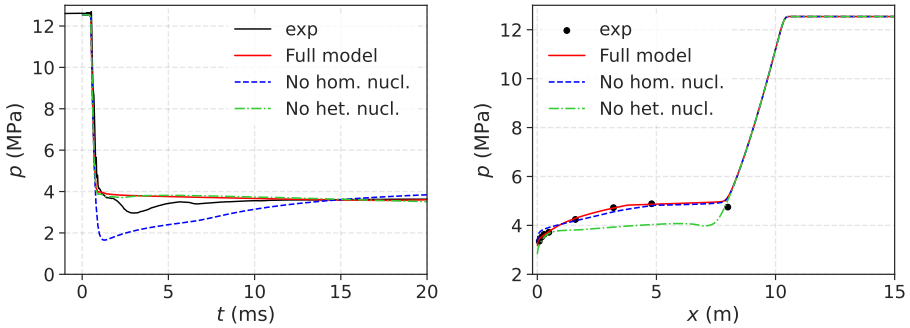

(a) Modeled and measured pressure at 28 cm from the open end of the pipe.

(b) Modeled and measured pressure along the pipe at t = 20 ms after disk rupture.

Figure 19: Investigation of the effect on the HFM when the homogeneous nucleation model or the heterogeneous nucleation model is omitted.

In Figure 19a, we show the pressure evolution at $x = 28$ cm for the complete HFM and for the HFM omitting either the homogeneous or the heterogeneous nucleation model. When homogeneous nucleation is omitted, the modeled pressure undershoot becomes much too large, and the pressure increases too quickly. Interestingly, ignoring the heterogeneous nucleation term provides nearly no difference in the resulting pressure prediction at $x = 28$ cm from the open end for the time frame considered here. This suggests that homogeneous nucleation dominates the flashing process close to the open end of the pipe for this depressurization case.

In Figure 19b, we show the pressure profile along the pipe at $t = 20$ ms for the complete HFM and for the HFM omitting either the homogeneous nucleation terms or the heterogeneous nucleation terms. Most interestingly, when heterogeneous nucleation is ignored, the pressure from $x > 1$ m and up to the position of the fast-moving rarefaction wave is underestimated by up to 1 MPa. In this region, the local superheat is too small for a significant amount of bubbles to nucleate homogeneously, so the two-phase mixture area is not accurately predicted. The heterogeneous term ensures that the two-phase flow extends further into the pipe.

Figure 20 shows the profile of the volume fraction of vapor 8 m along the pipe for the full HFM and the HFM where either homogeneous or heterogeneous nucleation is omitted. The recorded pressure profile at $t = 20$ ms suggests that there is two-phase flow up to around 4 m inside the pipe. The HFM without heterogeneous nucleation only predicts vapor 1.3 m into the pipe.

Based on the above results, we note the following on the effect of the homogeneous and heterogeneous nucleation terms on the pressure evolution inside the pipe:

- Homogeneous nucleation dominates near the open end of the pipe and limits the predicted pressure undershoot for the present case.
- Even though we are considering a relatively warm case, where homogeneous nucleation is expected to dominate, our results suggest that heterogeneous nucleation plays a major role in initiating (flash) boiling further inside the pipe.
- This means that both homogeneous and heterogeneous nucleation must be accurately accounted for to predict the flash boiling characteristics during pipe depressurizations of liquid CO_2 throughout the length of the pipe.

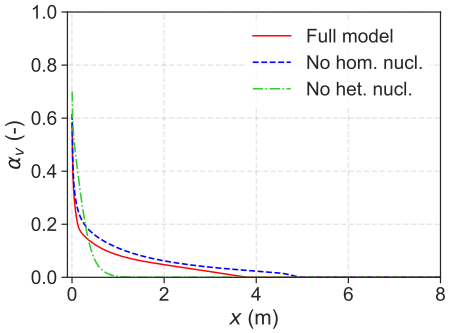

Figure 20: Modeled volume fraction of vapor inside the pipe for the complete HFM and when either homogeneous nucleation or heterogeneous nucleation is ignored.

6. Conclusions

Accurate models for flashing flows can improve the efficiency and safe operation of several industrial systems including nuclear cooling systems, refrigeration units and CO_2 pipeline transportation systems in the context of CCS. In the present work, we propose and study a homogeneous flashing model (HFM) for transient, flashing flow, in which the physical phenomena of the flashing are taken into account: homogeneous and heterogeneous bubble nucleation, coalescence, break-up and growth. The flow equations of the HFM are the same as for the homogeneous chemical potential-relaxation model (HRM*), with the addition of transport equations for the bubble density in the flow and total interfacial area between liquid and vapor. Homogeneous nucleation is modeled using classical nucleation theory and heterogeneous nucleation is modeled with constant rates for bubble creation and mass transfer from liquid to vapor.

We have fitted and compared the HFM to experimental data from eight full-bore CO_2 pipe depressurization tests conducted at temperatures from approximately 5 °C to 40 °C and a pressure of about 12 MPa. The results were also discussed in relation to those of the HRM* with a standard HRM-type mass-transfer model. The relaxation parameter in the HRM-type model was set using an empirical correlation that has been tuned on a case-by-case basis for each experiment. The effect of the homogeneous and heterogeneous nucleation models in the HFM was also investigated. The results are summarized below:

- The average mean absolute percentage error of the HFM fit to the pressure recordings for four pressure sensors close to the pipe's open end over 20 ms of the depressurization tests was 6.0%, and for the HRM* it was 7.6%.
- The HFM was tuned to the experimental data using parameters related to the heterogeneous nucleation and bubble breakup. The parameters were tuned to the first 20 ms of the experimental data by visual inspection. The same parameter values provided a reasonable fit for all the experiments, i.e., it was not necessary to tune the model on a case-by-case basis. The results suggest that incorporating homogeneous nucleation in the flashing flow model enhances the predictive capabilities of the model.
- The pressure evolution calculated by the HFM was investigated in more detail for the warmest (40 °C), coldest (5 °C) and an intermediate temperature (21 °C)

depressurization test from the experimental dataset. These experiments have very different flashing characteristics.

- For the warm and intermediate temperature depressurization tests, we found that homogeneous nucleation plays a main role in limiting the liquid superheat near the pipe's open end and heterogeneous nucleation plays a main role in initiating flashing further inside the pipe.

- For the coldest test, our results indicate that only heterogeneous nucleation caused flashing in the pipe. The HFM obtained a too low pressure near the open end for this case, suggesting that the constant-rate parameters for heterogeneous nucleation are too simple to capture the actual nucleation process.

- Heterogeneous nucleation must always be accounted for, both for cold and warm depressurization cases. If heterogeneous nucleation is neglected for warm cases, the pressure is underestimated further inside the pipe as homogeneous nucleation is not initiated there.

In summary, the HFM constitutes a promising step towards a fully predictive model for pipe depressurization with flashing.

Note that there are several interesting avenues for further work:

- In the present flow model, the temperatures of the phases are assumed to be equal, $T_v = T_\ell$, which is a simplification. The same mass-transfer model could be tested with flow models that allow for a temperature difference between the phases. This may improve the estimates of the evaporation/bubble growth model as well, as discussed in Section 5.2.1, which currently overestimates the mass transfer caused by evaporation.

- In order to improve the estimates of mass transfer caused by bubble growth, one may also test bubble growth models governed by heat transfer between the phases and/or the wall of the pipe.

- The model for heterogeneous nucleation in the HFM assumes constant rates of bubble nucleation and mass transfer. Although the model performed well for the cases considered here, this may not be the case in other situations or for longer times. As we have found heterogeneous nucleation to be essential in modeling the flashing inside the pipe for both cold and warm depressurization cases, more refined models for this kind of nucleation should be tested, accounting for, e.g., the activation of nucleation sites, bubble growth and bubble departure rate from these sites.

For the HFM to become fully predictive, an accurate model for heterogeneous bubble nucleation in real systems must be developed. To the authors' knowledge, such a model does not yet exist.

Acknowledgments

This publication has been produced with support from the NCCS Centre, performed under the Norwegian research programme Centres for Environment-friendly Energy Research (FME). The authors acknowledge the following partners for their contributions: Aker BP, Aker Carbon Capture, Allton, Ansaldo Energia, Baker Hughes,

CoorsTek Membrane Sciences, Elkem, Eramet, Equinor, Gassco, Hafslund Oslo Celsio, Krohne, Larvik Shipping, Norcem Heidelberg Cement, Offshore Norge, Quad Geometrics, Stratum Reservoir, TotalEnergies, Vår Energi, Wintershall Dea and the Research Council of Norway (257579).

The construction of the ECCSEL Depressurization Facility was supported by the INFRASTRUKTUR programme of the Research Council of Norway (225868).

We thank Dr. Kamal K. Botros for sharing data from CO_2 depressurization tests conducted at Nova chemicals. The data was used to estimate the points where flashing first occurred for these tests, as shown in Figure 6.

Data availability

The experimental data recorded in this study can be downloaded from Zenodo (Log *et al.*, 2023b). (The DOI will be activated at publication.) The data from the other tests conducted at the ECCSEL depressurization facility can also be downloaded from Zenodo (Munkejord *et al.*, 2020b; Log *et al.*, 2023a).

References

Aasen, A., Wilhelmsen, Ø., Hammer, M., Reguera, D., 2023. Free energy of critical droplets – from the binodal to the spinodal. *J. Chem. Phys.* 158 (11). doi:10.1063/5.0142533.

Alamgir, M., Lienhard, J. H., 1981. Correlation of Pressure Undershoot During Hot-Water Depressurization. *J. Heat Transfer* 103 (1), 52–55. doi:10.1115/1.3244429.

Angielczyk, W., Bartosiewicz, Y., Butrymowicz, D., 2020. Development of delayed equilibrium model for CO_2 convergent-divergent nozzle transonic flashing flow. *Int. J. Multiphase Flow* 131, 103351. doi:10.1016/j.ijmultiphaseflow.2020.103351.

Angielczyk, W., Bartosiewicz, Y., Butrymowicz, D., Seynhaeve, J.-M., 2010. 1-D modeling of supersonic carbon dioxide two-phase flow through ejector motive nozzle. In: *International Refrigeration and Air Conditioning Conference*. Purdue University. URL `https://docs.lib.purdue.edu/iracc/1102/`.

Angielczyk, W., Seynhaeve, J. M., Gagan, J., Bartosiewicz, Y., Butrymowicz, D., 2019. Prediction of critical mass rate of flashing carbon dioxide flow in convergent-divergent nozzle. *Chem. Eng. Process. – Process Intensif.* 143 (4), 107599. doi:10.1016/j.cep.2019.107599.

Apfel, R. E., 1970. The Role of Impurities in Cavitation-Threshold Determination. *J. Acoust. Soc. Am.* 48, 1179–1186. doi:10.1121/1.1912258.

Atchley, A. A., Prosperetti, A., 1989. The crevice model of bubble nucleation. *J. Acoust. Soc. Am.* 86, 1065–1084. doi:10.1121/1.398098.

Aursand, E., Dumoulin, S., Hammer, M., Lange, H. I., Morin, A., Munkejord, S. T., Nordhagen, H. O., 2016. Fracture propagation control in CO_2 pipelines: Validation of a coupled fluid-structure model. *Eng. Struct.* 123, 192–212. doi:10.1016/j.engstruct.2016.05.012.

Aursand, P., Gjennestad, M. A., Aursand, E., Hammer, M., Wilhelmsen, Ø., 2016. The spinodal of single- and multi-component fluids and its role in the development of modern equations of state. *Fluid Phase Equilib.* 436, 98–112. doi:10.1016/j.fluid.2016.12.018.

Aursand, P., Hammer, M., Lavrov, A., Lund, H., Munkejord, S. T., Torsæter, M., 2017. Well integrity for CO_2 injection from ships: Simulation of the effect of flow and material parameters on thermal stresses. *Int. J. Greenh. Gas Con.* 62, 130–141. doi:10.1016/j.ijggc.2017.04.007.

Banasiak, K., Hafner, A., 2013. Mathematical modelling of supersonic two-phase R744 flows through converging–diverging nozzles: The effects of phase transition models. *Appl. Therm. Eng.* 51 (1), 635–643. ISSN 1359-4311. doi:10.1016/j.applthermaleng.2012.10.005.

Bankoff, S. G., 1958. Entrapment of gas in the spreading of a liquid over a rough surface. *aichej* 4. doi:10.1002/aic.690040105.

Barták, J., 1990. A study of the rapid depressurization of hot water and the dynamics of vapour bubble generation in superheated water. *Int. J. Multiphase Flow* 16, 789–798. doi:10.1016/0301-9322(90)90004-3.

Bartosiewicz, Y., Seynhaeve, J.-M., 2013. Delayed equilibrium model (DEM) of flashing flows relevant to LOCA. *Multiphase Sci. Technol.* 25, 117–131. doi:10.1615/MultScienTechn.v25.i2-4.50.

Bartosiewicz, Y., Seynhaeve, J.-M., 2014. Delayed equilibrium model (DEM) of flashing choked flows relevant to LOCA and implementation in system codes. In: *Proceedings of the 2014 22nd International Conference on Nuclear Engineering*. Prague, Czech Republic, vol. Volume 2B: Thermal Hydraulics, p. V02BT09A040. doi:10.1115/ICONE22-30957.

Bejan, A., 1993. *Heat Transfer*. John Wiley & Sons, Inc., New York. ISBN 0-471-50290-1.

Bilicki, Z., Kestin, J., 1990. Physical Aspects of the Relaxation Model in Two-Phase Flow. In: *Proceedings of the Royal Society of London. Series A, Mathematical and Physical Sciences*. Royal Society, vol. 428, pp. 379–397. doi:10.1098/rspa.1990.0040.

Blinkov, V. N., Jones, O. C., Nigmatulin, B. I., 1993. Nucleation and flashing in nozzles – 2. Comparison with experiments using a five-equation model for vapor void development. *Int. J. Multiphase Flow* 19 (6), 965–986. doi:10.1016/0301-9322(93)90072-3.

Botros, K. K., Geerligs, J., Rothwell, B., Robinson, T., 2016. Measurements of decompression wave speed in pure carbon dioxide and comparison with predictions by equation of state. *J. Press. Vess. – T. ASME* 138 (3). doi:10.1115/1.4031941.

Botros, K. K., Geerligs, J., Rothwell, B., Robinson, T., 2017. Effect of argon as the primary impurity in anthropogenic carbon dioxide mixtures on the decompression wave speed. *Can. J. Chem. Eng.* 95 (3), 440–448. doi:10.1002/cjce.22689.

Botros, K. K., Geerligs, J., Rothwell, B., Robinson, T., 2017. Measurements of decompression wave speed in binary mixtures of carbon dioxide mixtures and impurities. *J. Press. Vess. – T. ASME* 139 (2). doi:10.1115/1.4034016.

Botros, K. K., Geerligs, J., Rothwell, B., Robinson, T., 2017. Measurements of decompression wave speed in simulated anthropogenic carbon dioxide mixtures containing hydrogen. *J. Press. Vess. – T. ASME* 139 (2). doi:10.1115/1.4034466.

Brown, S., Beck, J., Mahgerefteh, H., Fraga, E. S., 2013. Global sensitivity analysis of the impact of impurities on CO_2 pipeline failure. *Reliab. Eng. Syst. Safe* 115, 43–54. doi:10.1016/j.ress.2013.02.006.

Brown, S., Martynov, S., Mahgerefteh, H., Chen, S., Zhang, Y., 2014. Modelling the non-equilibrium two-phase flow during depressurisation of CO_2 pipelines. *Int. J. Greenh. Gas Con.* 30, 9–18. doi:10.1016/j.ijggc.2014.08.013.

Brownsort, P., 2019. *Briefing on carbon dioxide specifications for transport*. Tech. rep., CCUS Projects Network, EU. URL `https://www.ccusnetwork.eu/sites/default/files/TG3_Briefing-CO2-Specifications-for-Transport.pdf`. Accessed 2023-10-17.

Chappell, M. A., Payne, S. J., 2007. The effect of cavity geometry on the nucleation of bubbles from cavities . *J. Acoust. Soc. Am.* 121, 853 – 862. doi:10.1121/1.2404629.

Committee on Carbon Capture, Use, and Storage, 2019. *Meeting the Dual Challenge: A Roadmap to At-Scale Deployment of Carbon Capture, Use, and Storage: Volume III – Analysis of CCUS Technologies*. Tech. rep., National Petroleum Council. URL `https://dualchallenge.npc.org/downloads.php`. Accessed 2023-10-17.

Cosham, A., Jones, D. G., Armstrong, K., Allason, D., Barnett, J., 2014. Analysis of two dense phase carbon dioxide full-scale fracture propagation tests. In: *10th International Pipeline Conference, IPC2014*. Calgary, Canada, vol. 3. doi:10.1115/IPC2014-33080.

De Lorenzo, M., Lafon, P., Seynhaeve, J.-M., Bartosiewicz, Y., 2017. Benchmark of delayed equilibrium model (DEM) and classic two-phase critical flow models against experimental data. *Int. J. Multiphase Flow* 92, 112–130. doi:10.1016/j.ijmultiphaseflow.2017.03.004.

Debenedetti, P. G., 1997. *Metastable Liquids: Concepts and Principles*. Princeton University Press. ISBN 9780691213941. doi:10.1515/9780691213941.

Deligiannis, P., Cleaver, J., 1990. The role of nucleation in the initial phases of a rapid depressurization of a subcooled liquid. *Int. J. Multiphase Flow* 16 (6), 975–984. doi:10.1016/0301-9322(90)90102-O.

Deligiannis, P., Cleaver, J., 1992. Determination of the heterogeneous nucleation factor during a transient liquid expansion. *Int. J. Multiphase Flow* 18 (2), 273–278. doi:10.1016/0301-9322(92)90088-X.

DNV, 2021. Design and operation of carbon dioxide pipelines, recommended practise. DNV-RP-F104.

Downar-Zapolski, P., Bilicki, Z., Bolle, L., Franco, J., 1996. The non-equilibrium relaxation model for one-dimensional flashing liquid flow. *Int. J. Multiphase Flow* 22 (3), 473–483. doi:10.1016/0301-9322(95)00078-X.

ECCSEL, 2021. Depressurization facility. `https://www.eccsel.org/catalogue/113`. Accessed 2023-05-23.

Edwards, A. R., O'Brien, T. P., 1970. Studies of phenomena connected with the depressurization of water reactors. *The Journal of the British Nuclear Energy Society* 9 (2), 125–135.

Elias, E., Chambré, P. L., 1993. Flashing Inception in Water During Rapid Decompression. *J. Heat Transfer* 115 (1), 231–238. doi:10.1115/1.2910654.

Flechas, T., Laboureur, D. M., Glover, C. J., 2020. A 2-D CFD model for the decompression of carbon dioxide pipelines using the Peng-Robinson and the Span-Wagner equation of state. *Process Saf. Environ.* 140, 299–313. doi:10.1016/j.psep.2020.04.033.

Friedel, L., 1979. Improved friction pressure drop correlations for horizontal and vertical two phase pipe flow. In: *Proceedings, European Two Phase Flow Group Meeting*. Ispra, Italy. Paper E2.

Gallo, M., Magaletti, F., Casciola, C. M., 2021. Heterogeneous bubble nucleation dynamics. *J. Fluid Mech.* 906, A20. doi:10.1017/jfm.2020.761.

Gungor, K. E., Winterton, R. H. S., 1987. Simplified general correlation for saturated flow boiling and comparisons of correlations with data. *Chem. Eng. Res. Des.* 65 (2), 148–156.

Hammer, M., Aasen, A., Wilhelmsen, Ø., 2023. Thermopack. `https://github.com/thermotools/thermopack`. Accessed 2023-06-14.

Hammer, M., Deng, H., Austegard, A., Log, A. M., Munkejord, S. T., 2022. Experiments and modelling of choked flow of CO_2 in orifices and nozzles. *Int. J. Multiphase Flow* 156, 104201. doi:10.1016/j.ijmultiphaseflow.2022.104201.

Hansen, P. M., Gaathaug, A. V., Bjerketvedt, D., Vågsæther, K., 2019. Rapid depressurization and phase transition of CO_2 in vertical ducts – small-scale experiments and rankine-hugoniot analyses. *J. Hazard. Mater.* 365, 16–25. doi:10.1016/j.jhazmat.2018.10.092.

Hesketh, R. P., Fraser Russel, T. W., Etchells, A. W., 1987. Bubble size in horizontal pipelines. *AIChE Journal* 33 (4), 663–667. doi:10.1002/aic.690330414.

Hibiki, T., Ishii, M., 2003. Active nucleation site density in boiling systems. *Int. J. Heat Mass Tran.* 46 (14), 2587–2601. doi:10.1016/S0017-9310(03)00031-0.

IPCC, 2005. *IPCC Special Report on Carbon Dioxide Capture and Storage. Prepared by Working Group III of the Intergovernmental Panel on Climate Change*. IPCC, Cambridge University Press, Cambridge, United Kingdom and New York, NY, USA. URL `https://www.ipcc.ch/site/assets/uploads/2018/03/srccs_wholereport-1.pdf`. Accessed 2023-10-17.

Ivashnyov, O. E., Ivashneva, M. N., Smirnov, N. N., 2000. Slow waves of boiling under hot water depressurization. *J. Fluid Mech.* 413, 149–180. doi:10.1017/S0022112000008417.

Kjelstrup, S., Bedeaux, D., 2008. *Non-equilibrium thermodynamics of heterogeneous systems*. World Scientific. doi:10.1142/6672.

Klinkby, L., Nielsen, C. M., Krogh, E., Smith, I. E., Palm, B., Bernstone, C., 2011. Simulating rapidly fluctuating CO_2 flow into the Vedsted CO_2 pipeline, injection well and reservoir. In: Gale, J., Hendriks, C., Turkenberg, W. (Eds.), *GHGT-10 – 10th International Conference on Greenhouse Gas Control Technologies*. IEAGHGT, Energy Procedia vol. 4, Amsterdam, The Netherlands, pp. 4291–4298. doi:10.1016/j.egypro.2011.02.379.

Kocamustafaogullari, G., Ishii, M., 1983. Interfacial area and nucleation site density in boiling systems. *Int. J. Heat Mass Tran.* 26 (9), 1377–1387. doi:10.1016/S0017-9310(83)80069-6.

Kunz, O., Wagner, W., 2012. The GERG-2008 wide-range equation of state for natural gases and other mixtures: An expansion of GERG-2004. *J. Chem. Eng. Data* 57 (11), 3032–3091. doi:10.1021/je300655b.

Le Martelot, S., Saurel, R., Nkonga, B., 2014. Towards the direct numerical simulation of nucleate boiling flows. *Int. J. Multiphase Flow* 66, 62–78. doi:10.1016/j.ijmultiphaseflow.2014.06.010.

Lee, W. H., 1980. A pressure iteration scheme for two-phase flow modeling. In: Veziroglu, T. N. (Ed.), *Multiphase Transport Fundamentals,Reactor Safety, Applications*, Hemisphere Publishing Corporation, Washington DC. doi:10.1142/9789814460286_0004.

LeVeque, R. J., 2002. *Finite Volume Methods for Hyperbolic Problems*. Cambridge University Press, Cambridge, UK. ISBN 0-521-00924-3.

Levich, V. G., 1962. *Physicochemical Hydrodynamics*. Prentice-Hall, Englewood Cliffs, N.J. ISBN 0136744400.

Liao, Y., Lucas, D., 2017. Computational modelling of flash boiling flows: A literature survey. *Int. J. Heat Mass Tran.* 111, 246–265. doi:10.1016/j.ijheatmasstransfer.2017.03.121.

Liao, Y., Lucas, D., 2017. Possibilities and Limitations of CFD Simulation for Flashing Flow Scenarios in Nuclear Applications. *Energy* 10. doi:10.3390/en10010139.

Liao, Y., Lucas, D., 2021. A review on numerical modelling of flashing flow with application to nuclear safety analysis. *Appl. Therm. Eng.* 182, 116002. doi:10.1016/j.applthermaleng.2020.116002.

Lienhard, J. H., Alamgir, M., Trela, M., 1978. Early response of hot water to sudden release from high pressure. *J. Heat Trans. – T. ASME* 100 (3), 473–479. doi:10.1115/1.3450833.

Liu, B., Liu, X., Lu, C., Godbole, A., Michal, G., Tieu, A. K., 2017. Multi-phase decompression modeling of CO_2 pipelines. *Greenh. Gas. Sci. Tech.* 7 (4), 665–679. doi:10.1002/ghg.1666.

Liu, B., Liu, X., Lu, C., Godbole, A., Michal, G., Tieu, A. K., 2018. A CFD decompression model for CO_2 mixture and the influence of non-equilibrium phase transition. *Appl. Energ.* 227, 516–524. doi:10.1016/j.apenergy.2017.09.016.

Log, A. M., Hammer, M., Deng, H., Austegard, A., Hafner, A., Munkejord, S. T., 2023. Depressurization of CO_2 in pipes: Effect of initial state on non-equilibrium two-phase flow – dataset. Zenodo. doi:10.5281/zenodo.7669536.

Log, A. M., Hammer, M., Deng, H., Austegard, A., Hafner, A., Munkejord, S. T., 2024. Depressurization of CO_2 in pipes: Effect of initial state on non-equilibrium two-phase flow. *Int. J. Multiphase Flow* 170, 104624. doi:10.1016/j.ijmultiphaseflow.2023.104624.

Log, A. M., Hammer, M., Munkejord, S. T., 2023. A flashing flow model for the rapid depressurization of CO_2 in a pipe accounting for bubble nucleation and growth – dataset. Zenodo. doi:10.5281/zenodo.8164913.

Log, A. M., Munkejord, S. T., Hammer, M., Hafner, A., Deng, H., Austegard, A., 2022. Investigation of non-equilibrium effects during the depressurization of carbon dioxide. In: *15th IIR-Gustav Lorentzen Conference on Natural Refrigerants (GL2022). Proceedings. Trondheim, Norway, June 13-15th 2022*. International Institute of Refrigeration (IIR). doi:10.18462/iir.gl2022.0197.

Lund, H., 2012. A hierarchy of relaxation models for two-phase flow. *SIAM J. Appl. Math.* 72 (6), 1713–1741. doi:10.1137/12086368X.

Michal, G., Østby, E., Davis, B. J., Røneid, S., Lu, C., 2020. An empirical fracture control model for dense-phase CO2 carrying pipelines. In: *13th International Pipeline Conference, IPC 2020*. ASME. doi:10.1115/IPC2020-9421.

Munkejord, S. T., Austegard, A., Deng, H., Hammer, M., Stang, H. G. J., Løvseth, S. W., 2020. Depressurization of CO_2 in a pipe: High-resolution pressure and temperature data and comparison with model predictions. *Energy* 211, 118560. doi:10.1016/j.energy.2020.118560.

Munkejord, S. T., Austegard, A., Deng, H., Hammer, M., Stang, H. G. J., Løvseth, S. W., 2020. Depressurization of CO_2 in a pipe: High-resolution pressure and temperature data and comparison with model predictions – dataset. Zenodo. doi:10.5281/zenodo.3928227.

Munkejord, S. T., Deng, H., Austegard, A., Hammer, M., Skarsvåg, H. L., Aasen, A., 2021. Depressurization of CO_2-N_2 and CO_2-He in a pipe: Experiments and modelling of pressure and temperature dynamics. *Int. J. Greenh. Gas Con.* 109, 103361. doi:10.1016/j.ijggc.2021.103361.

Munkejord, S. T., Hammer, M., Løvseth, S. W., 2016. CO_2 transport: Data and models – A review. *Appl. Energ.* 169, 499–523. doi:10.1016/j.apenergy.2016.01.100.

Nakagawa, M., Berana, M. S., Kishine, A., 2009. Supersonic two-phase flow of CO_2 through converging-diverging nozzles for the ejector refrigeration cycle. *Int. J. Refrig.* 32 (6), 1195–1202. doi:10.1016/j.ijrefrig.2009.01.015.

Pelanti, M., 2022. Arbitrary-rate relaxation techniques for the numerical modeling of compressible two-phase flows with heat and mass transfer. *Int. J. Multiphase Flow* 153, 104097. doi:10.1016/j.ijmultiphaseflow.2022.104097.

Pelanti, M., Shyue, K.-M., 2014. A mixture-energy-consistent six-equation two-phase numerical model for fluids with interfaces, cavitation and evaporation waves. *J. Comput. Phys.* 259, 331–357. doi:10.1016/j.jcp.2013.12.003.

Pham, L. H. H. P., Rusli, R., 2016. A review of experimental and modelling methods for accidental release behaviour of high-pressurised CO_2 pipelines at atmospheric environment. *Process Saf. Environ.* 104, 48–84. doi:10.1016/j.psep.2016.08.013.

Pinhasi, G. A., Ullmann, A., Dayan, A., 2005. Modeling of flashing two-phase flow. *Reviews in Chemical Engineering* 21 (3-4), 133–264. doi:10.1515/REVCE.2005.21.3-4.133.

Quinn, D., Stannard, D., Edwards, J., Botros, K. K., Johansen, C., 2022. Experimental visualization and characteristics of bubble nucleation during rapid decompression of supercritical and subcooled carbon dioxide. *Int. J. Pres. Ves. Pip.* 195, 104569. doi:10.1016/j.ijpvp.2021.104569.

Rathjen, W., Straub, J., 1977. Temperature dependence of surface tension, coexisting curve, and vapor pressure of CO_2, $CClF_3$, $CBrF_3$, and SF_6. In: Hahne, E., Grigull, U. (Eds.), *Heat Transfer in Boiling*, Taylor & Francis Inc., chap. 18. ISBN 0-123-14450-7.

Ringstad, K. E., Allouche, Y., Gullo, P., Ervik, Ã., Banasiak, K., Hafner, A., 2020. A detailed review on CO_2 two-phase ejector flow modeling. *Therm. Sci. Eng. Prog.* 20, 100647. doi:10.1016/j.tsep.2020.100647.

Riznic, J. R., Ishii, M., 1989. Bubble number density and vapor generation in flashing flow. *Int. J. Heat Mass Tran.* 32 (10), 1821–1833. doi:10.1016/0017-9310(89)90154-3.

Saha, K., Som, S., Battistoni, M., 2017. Investigation of homogeneous relaxation model parameters and their implications for gasoline injectors. *At. Sprays* 27, 345–365. doi:10.1615/AtomizSpr.2017016338.

Saurel, R., Petitpas, F., Abgrall, R., 2008. Modelling phase transition in metastable liquids: application to cavitating and flashing flows. *J. Fluid Mech.* 607, 313–350. doi:10.1017/S0022112008002061.

Seynhaeve, J.-M., Crécy, A. D., Bartosiewicz, Y., 2015. Uncertainty analysis of delayed equilibrium model (dem) using the circe methodology. In: *NURETH16*. Chicago, USA. URL `https://glc.ans.org/nureth-16/data/papers/12971.pdf`. Accessed 2023-07-30.

Shin, T. S., Jones, O. C., 1993. Nucleation and flashing in nozzles – 1. A distributed nucleation model. *Int. J. Multiphase Flow* 19 (6), 943–964. doi:10.1016/0301-9322(93)90071-2.

Skarsvåg, H. L., Hammer, M., Munkejord, S. T., Log, A. M., Dumoulin, S., Gruben, G., 2023. Towards an engineering tool for the prediction of running ductile fractures in CO_2 pipelines. *Process Saf. Environ.* 171, 667–679. doi:10.1016/j.psep.2023.01.054.

Toro, E. F., Spruce, M., Speares, W., 1994. Restoration of the contact surface in the HLL-Riemann solver. *Shock Waves* 4 (1), 25–34.

Wilhelmsen, Ø., Aasen, A., 2022. Choked liquid flow in nozzles: Crossover from heterogeneous to homogeneous cavitation and insensitivity to depressurization rate. *Chem. Eng. Sci.* 248, 117176. doi:10.1016/j.ces.2021.117176.

Wilhelmsen, Ø., Aasen, A., Skaugen, G., Aursand, P., Austegard, A., Aursand, E., Gjennestad, M. A., Lund, H., Linga, G., Hammer, M., 2017. Thermodynamic modeling with equations of state: Present challenges with established methods. *Ind. Eng. Chem. Res.* 56 (13), 3503–3515. doi:10.1021/acs.iecr.7b00317.

Wilt, P. M., 1986. Nucleation rates and bubble stability in water-carbon dioxide solutions. *J. Colloid Interf. Sci.* 112 (2), 530–538. doi:10.1016/0021-9797(86)90122-0.

Winters, W. S., Jr., Merte, J. H., 1979. Experiments and Nonequilibrium Analysis of Pipe Blowdown. *Nucl. Sci. Eng.* 69 (3), 411–429. doi:10.13182/NSE79-A19959.

Xiao, C., Lu, Z., Yan, L., Yao, S., 2020. Transient behaviour of liquid CO_2 decompression: CFD modelling and effects of initial state parameters. *Int. J. Greenh. Gas Con.* 101, 103154. doi:10.1016/j.ijggc.2020.103154.